

Storage of Charge in Redox Conductive Polymers Probed with Electron Spin Resonance Spectroscopy

Ilia Romanovich Kulikov

Im Fachbereich Physik der Freien Universität Berlin eingereichte
Dissertation zur Erlangung des Grades eines
Doktors der Naturwissenschaften

Berlin
August 2023

Erster Gutachter: Prof. Dr. Jan Behrends
Zweiter Gutachter: Prof. Dr. Kirill Bolotin
Tag der Disputation:

Contents

1	Introduction	7
2	Electrochemical Energy Storage in Redox Conductive Polymers	11
2.1	Rechargeable Electrochemical Cells	11
2.2	Redox Conductive Polymers	11
2.3	Organic Radical Battery	12
2.4	Organic Electrode Materials	12
2.4.1	TEMPO	12
2.4.2	PTMA	13
2.4.3	NiSalen	13
2.4.4	pDiTBuS	13
2.4.5	pDiTS	14
2.4.6	Density Functional Theory Calculation of Spin Density on DiTS .	14
2.4.7	Charge Transport Model for Redox Conductive Polymers	14
3	Operando EPR Spectroscopy of TEMPO-Salen Electrochemical Cells	17
3.1	Electron Paramagnetic Resonance	17
3.1.1	The Spin Hamiltonian	17
3.1.2	cwEPR spectroscopy	20
3.2	cwEPR Spectroscopy of TEMPO Containing Molecular Fragments	23
3.2.1	Room Temperature Spectra of TEMPO [•] Solutions	23
3.2.2	Spectra of TEMPO [•] /TEMPO ⁺ Films	26
3.2.3	Spectra of NiSalen Films	27
3.3	cwEPR Spectroscopy of a Charging Electrochemical Cell	27
3.3.1	Fabrication of EPR-compatible Electrochemical Cells	29
3.4	Versatile electrode setup for ex-situ and in-situ spectroelectrochemical EPR	29
3.4.1	Fabrication of the modified tube	30

3.4.2	Q-factors and cwEPR spectra for p-DiTS in standard and modified tube	31
3.4.3	cwEPR Spectra During a Charge-Discharge Cycle	32
3.4.4	Spectral Simulations	33
3.4.5	Quantitative Analysis of Potential-Dependent EPR Spectra	33
3.4.6	EPR-Detected State Of Charge	33
3.4.7	Formation of Singlet Spin States in a Reduced Cathode Film	33
3.4.8	Monitoring of Degradation Processes	33
3.4.9	Monitoring of Self Discharge	34
3.4.10	Electrochemical Cells with Solid Electrolyte	34
3.4.11	Low Temperature Measurements	34
4	Pulsed EPR Spectroscopy of TEMPO-containing Battery Cathodes	49
4.1	Coherent Spin Motion under Pulsed Microwave Field	49
4.1.1	Bloch Equations	49
4.1.2	Spin Relaxation Times	49
4.1.3	Spin Packets	49
4.2	Instrumentation	49
4.2.1	Pulse Sequences and Measurement Techniques	49
4.2.2	Broad-Band Excitation and Instantaneous Diffusion	51
4.3	Pulsed EPR Spectroscopy of a charged pDiTBuS Cathode film	52
4.3.1	Field Swept Echo of a charged pDiTBuS Cathode film	52
4.3.2	Estimation of Local Spin Concentrations with Instantaneous Diffusion	52
4.3.3	Spin Relaxation in a charged pDiTBuS Cathode Film	52
4.4	Padé-Laplace Deconvolution of Polyexponential Decay Signals	52
4.4.1	Padé-Laplace Deconvolution of the Echo-Decay and Inversion-Recovery Transients	55
4.4.2	Detection of Domains with Poor Conductivity	62
4.4.3	Towards Electron Resonance Imaging of Spin Concentrations in Battery Electrodes	62
5	Conclusions and Outlook	65

$\vec{e}_x, \vec{e}_y, \vec{e}_z, t$	Laboratory frame of reference
$\vec{\hat{S}} = (\hat{S}_x, \hat{S}_y, \hat{S}_z)$	Spin operator
$h = 6.62607015 \times 10^{-34} \text{ J} \times \text{s}$	Planck constant
$g_e = -2.00231930436118(27)$	Electron g factor
$\mu_B = 9.2740100783(28) \times 10^{-24} \text{ J/T}$	Bohr magneton
$h = 1.25663706212(19) \times 10^{-6} \text{ N/A}^2$	Permeability of free space
ϵ	Relative permittivity
$\vec{B}_0 = B_0 \vec{e}_z$	Static magnetic field
cwEPR	Continuous wave electron paramagnetic resonance
pEPR	Pulsed electron paramagnetic resonance
EDMR	Electrically detected magnetic resonance
DUT	Device under testing
ORB	Organic radical battery
WE	Working electrode (cathode, "+")
CE	Counter electrode (anode, "-")
RE	Reference electrode
SoC	State of charge
ESOC	EPR-detected SoC
CV	Cyclic voltammogram
GCD	Galvanostatic charge-discharge
TEMPO	2,2,6,6-tetramethylpiperidine-1-oxyl
pDiTS	Poly-di-TEMPO-Salen
pDiTBU _S	Poly-di-TEMPO-Butyl-Salen
PTMA	Poly-TEMPO-methacrylate
EDFS	Echo-detected field sweep
ID	Instantaneous diffusion
T_1	Spin-lattice relaxation time
T_m	Phase memory time
t_d	Microwave detector dead time

Table 1: List of abbreviations

Chapter 1

Introduction

Life needs energy to continue its spread. Plants use photosynthesis to separate carbon from oxygen and to grow. Higher life forms as humans consume energy during the day and during the night, being dependent on the available energy source [?]. While fossil fuels are still the major source of energy [?] and while fire is used to convert the Joules that hold together hydrocarbon molecules into a "horse power" of a combustion engine and kilowatt-hours in a power socket, there are cleaner and more efficient ways to harvest energy. Photosynthesis had inspired the creation of solar panels that convert the sunlight into electricity, the atom had been tamed in the core of a nuclear reactor to power cities; we can extract energy from sound [?], wind and waves and from the heat of the planet. Moreover, there are hopes and continuous attempts to achieve nuclear fusion [?] - the creation of an artificial Sun by melting together atomic cores - the virtually inexhaustible and clean source of energy. The oil and gas are limited and unevenly distributed resources, wind does not always blow, the Sun does not shine at night, the wild Nature is still unpredictable and the extracted energy has to be stored in order to level out its production and consumption.

With the rise of the technological era, over the last century, energy has been delivered to our homes in form of electricity. Energy storage systems such as fuel cells, supercapacitors and batteries are crucial elements for powering portable electronics and vehicles, or for balancing a power grid with a renewable energy source. [27]. Two opposite electric charges separated from each other can store energy in an electrostatic field. It is possible to accumulate many charges on the plates of a capacitor and store some energy [?], but due to the technological difficulties, electrochemical cells are commonly used instead. An electrochemical cell is an energy storage device and a power source that undergoes a

chemical reaction to transfer some electric charge from one of its components to another through an external circuit. A simple electrochemical cell consists of three elements: two spatially separated materials called electrodes, and a solution of mobile ions between them called electrolyte. The two electrodes have different work functions, or, chemically speaking, reduction-oxidation (redox) potentials. When the electrodes of the cell are connected through an external circuit, the electrons flow through the circuit and the ions in the electrolyte rearrange to maintain charge balance [49]. While the cell delivers the electric current to the circuit, a chemical reaction is happening on its electrodes: the positively charged electrode, called cathode, is being reduced, obtaining electrons from the negatively charged anode through the external circuit. The anode loses electrons and is being oxidized. If the electrodes can undergo a reversible redox reaction, a current applied to the cell restores its charged state. The speed, reversibility, released by-products and physical conditions of this redox reaction are the key factors that define the charging rate, cycling stability, the self-discharge rate and the area of application of an electrochemical cell. This type of redox reaction had been of great interest for the field of energy storage, particularly, electrochemistry [?], where numerous characterization techniques have been developed to optimize the architecture of electrochemical power sources. Depending on the redox potentials of the used electrodes, the output voltage of a cell ranges between 0 and 5 V. Most applications require higher voltages, so multiple cells are connected in series to form a battery.

Stable, capacious and powerful batteries have become of great demand for today's energy driven society [79, 78, 55]. The advances in lithium ion technology for rechargeable batteries have enabled energy densities that make it possible to battery-power a wearable Internet-of-things device [40, 46], an airplane [31] or a house [11, 25]. Still, the application of lithium ion batteries is limited by irreversible processes [38, 19, 84] that occur upon extreme operating conditions such as high power demand [83, 23] or over-discharge [45]. Such degradation processes limit the performance of a battery by lowering its safe operating power, resulting in lower power density and longer charging times. The challenge to overcome these limitations, together with low abundance of Lithium, Cobalt and rare earth metals, [78, 27] and the toxicity of the manufacturing process [60, 58] is motivating research and development of advanced battery technologies [10]. This requires understanding of charge transport and degradation pathways in energy storage materials as well as exploring novel materials such as materials based on organic precursors [44, 33].

The flexible molecular design together with questions regarding unresolved charge transport- and performance limiting mechanisms have inspired a variety of characterization tech-

niques to be developed and applied to both energy storage materials and energy storage devices, operando and ex-situ. Together with electrochemical characterization as the standard method for studying the properties of energy storage materials[71, 82], operando optical microscopy [48], neutron imaging [45] and X-ray diffraction [61] were applied to monitor irreversible structural deformations during extreme charging of Li cells.

UV and IR spectroscopy turned out to be particularly useful for studying organic energy-storage materials. For instance, it was possible to observe formation of positive polarons in the NiSalen backbone of the pDiTBuS upon its oxidation [12]. Since the electrochemical processes happen within the bulk of the energy storage material and involve changes in the spin states, imaging techniques based on magnetic resonance can be applied to obtain structural information on the battery electrodes on the molecular level [52, 47, 41, 3]. NMR was used to study dendrite formation, electrolyte dynamics and intercalation of Li ions[37, 22] in Li cells, including operando imaging [68].

Operando continuous-wave EPR (cwEPR) was applied to study redox kinetics of inorganic battery cathodes [51], radical formation and spin densities in redox polymers [12] and in organic electrochemical cells [26, 35].

Pulsed EPR (pEPR) provides an even more powerful toolbox for material studies with the electron spin as a microscopic structural probe. In particular, pEPR provides access to the dipolar coupling between neighboring electron spins and thus the possibility to determine distances between adjacent redox-active centers using dipolar spectroscopy [63] as in spin-labelled proteins [30, 72]. In addition, the hyperfine coupling between electron and nuclear spins in close vicinity can be measured by electron spin echo envelope modulation (ESEEM) and electron nuclear double resonance (ENDOR) techniques and can thus elucidate the degree of delocalization for charge carriers in ORB materials in a similar way as in organic semiconductors [15].

Chapter 2

Electrochemical Energy Storage in Redox Conductive Polymers

2.1 Rechargeable Electrochemical Cells

The capacity of installed battery storage systems is predicted to increase upto 400 GWh by 2030 [17].

State of charge (SoC).

2.2 Redox Conductive Polymers

Redox active macromolecules or polymers [70] are known since 1940s due to the work of Lauth [?] and Cassidy [9] on electron exchange polymers. After the discovery of the conductivity of polyacetylene by Shirakawa, Heeger and McDiarmid in 1977 [69], polymers with sufficient charge transport were synthesized [] and the field of organic electronics had emerged and expanded.

The key for polymer conductivity is the p π - conjugated network, a system of overlapping π orbitals of carbon in a chain of alternating single and double carbon-carbon bonds that allows charge delocalization along the polymer backbone. An example of a π conjugated network is polyacetylene. Polyacetylene exhibits a band structure in the electron energy levels (between π and π^* orbitals) and represents a molecular semiconductor.

Organic solar cells [39] and organic field effect transistors [34] contain conjugated polymers that have electrical properties of semiconductors, yet can be easily printed in form of thin flexible films without using high temperatures. Combining the conductive polymers with stable radical side groups has formed the class of redox conductive poly-

mers and lead to the concept of an organic radical battery [62].

2.3 Organic Radical Battery

Batteries based on conjugated polymers containing stable radical moieties as high-capacitance groups represent a promising class of future electrochemical power sources - organic radical batteries (ORB) [50, 53, 76, ?]. ORB combine the advantages of high-power supercapacitors, namely high discharge rates, and the high energy density of conventional lithium-ion technology. In contrast to the lithium-ion battery, the charging of an organic battery does not involve intercalation of metal ions into the electrodes. This reduces the structural change of the electrode upon repeated recharging which allows for a longer cycle life of an ORB. The semi-conducting nature of organic electrodes reduces the Joule heating during the battery operation, and this allows for higher charge/discharge rates. The amorphous and swollen structure of organic electrodes allows the electrolyte ions to diffuse faster into the electrode, which also increases the charge/discharge rate [54]. A further beneficial property of organic materials over traditional inorganic materials is their availability and the low cost of the starting materials for the synthesis of the target polymers in conjunction with good mechanical properties [27, 49, 18]. The large knowledge base on polymer processing allows for inkjet printing, roll-to-roll processing and other low-cost manufacturing techniques for making low-cost, flexible and light-weight integrated devices, including flexible plastic batteries [27, 54].

2.4 Organic Electrode Materials

ORB based on redox polymers containing stable radicals [50] have been shown to compete with or even outperform conventional Li based batteries in terms of power densities [71] with the additional benefit of being free from rare precursors, inheriting mechanical properties of plastics and electrical properties of semiconductors [18, 7, 21]. Advanced molecular design techniques allow for tuning of the electrochemical properties of the redox polymers [28], that brings in a rich variety of organic energy storage materials [77, 74, 29] and creates a large room for their optimization.

2.4.1 TEMPO

TEMPO (2,2,6,6-tetramethylpiperidine-1-oxyl) shown in Figure ?? is a small molecule and a stable radical that can undergo a fast and reversible redox reaction between TEMPO^\bullet and TEMPO^+ . TEMPO is an inexpensive organic compound [74] produced from acetone

with liquid ammonia, hydrazine and peroxide [8]. TEMPO radicals are widely used as spin labels in biological systems.

Redox conductive conjugated polymers containing TEMPO redox groups, as pDiTBuS (poly-di-TEMPO-Butyl-Salen) shown in Figure 2.1, demonstrate particularly promising energy and power densities [73]. The pDiTBuS was designed as a cathode material: it is oxidized when the electrochemical cell containing this material is charged. A film of pDiTBuS comprises a high concentration of redox active stable nitroxyl radicals attached to a conjugated polymer backbone that interconnects them as a molecular wire. Such system can be viewed as a highly disordered molecular hole-transporting semiconductor (the poly-NiSalen backbone) that contains a large amount of hole traps (TEMPO groups) attached to it with butyl linkers. When the film is reduced (discharged), the TEMPO groups are in the radical state and act as unfilled traps. Upon oxidation (charging), the TEMPO fragments lose an unpaired electron and acquire a positive charge, so the traps are being filled with holes. The reversible redox reaction in the pDiTBuS film is demonstrated in a cyclic voltammogram shown in Figure ?? (see ESI).

While active electrode materials with nitroxide radicals as redox-active groups are ideally suited for organic radical batteries (ORBs) that exhibit high power densities, the broad application of most nitroxide-based materials is limited by their moderate electrical properties. A promising route towards overcoming the conductivity problem is the use of polymers that combine radical-containing moieties and a conductive backbone. This strategy was successfully followed in a number of studies focusing on different polymers.[?, 2, ?, ?, 1, ?]

The flexible molecular design together with questions regarding unresolved charge transport- and performance limiting mechanisms have inspired a variety of characterization techniques to be developed and applied to both energy storage materials and energy storage devices, operando and ex-situ. Together with electrochemical characterization as the standard method for studying the properties of energy storage materials[71, 82], operando optical microscopy [48], neutron imaging [45] and X-ray diffraction [61] were applied to monitor irreversible structural deformations during extreme charging of Li cells.

2.4.2 PTMA

2.4.3 NiSalen

2.4.4 pDiTBuS

Redox conductive conjugated polymers containing TEMPO (2,2,6,6-tetramethylpiperidine-1-oxyl) redox groups, as pDiTBuS (poly-di-TEMPO-Butyl-Salen) shown in Figure 2.1, demonstrate particularly promising energy and power densities [73]. The pDiTBuS was

designed as a cathode material: it is oxidized when the electrochemical cell containing this material is charged. A film of pDiTBuS comprises a high concentration of redox active stable nitroxyl radicals attached to a conjugated polymer backbone that interconnects them as a molecular wire. Such system may be viewed as a highly disordered molecular hole-transporting semiconductor (the poly-NiSalen backbone) that contains a large amount of hole traps (TEMPO groups) attached to it with butyl linkers. When the film is reduced (discharged), the TEMPO groups are in the radical state and act as unfilled traps. Upon oxidation (charging), the TEMPO fragments lose an unpaired electron and acquire a positive charge, so the traps are being filled with holes.

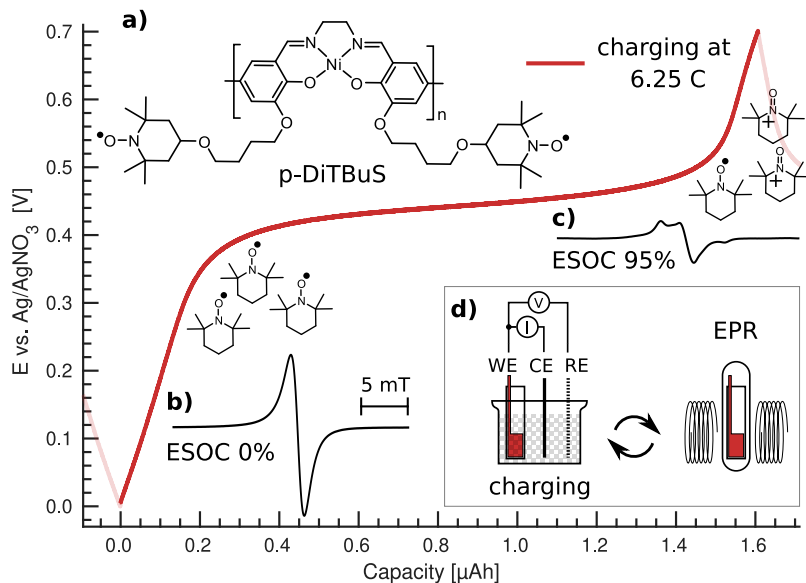


Figure 2.1: Galvanostatic charge-discharge curve for a pDiTBuS cathode film at 10 μ A (6.25 C), chemical structure of pDiTBuS (a), normalized cwEPR spectral signatures for reduced (b) and oxidized (c) states. Scheme of the ex-situ EPR measurement on the pDiTBuS half cell (d).

2.4.5 pDiTS

2.4.6 Density Functional Theory Calculation of Spin Density on DiTS

2.4.7 Charge Transport Model for Redox Conductive Polymers

A transfer of charge in a highly disordered molecular system, such as a film of a conjugated polymer, can be described in terms of hopping of charge carriers between the intertwined

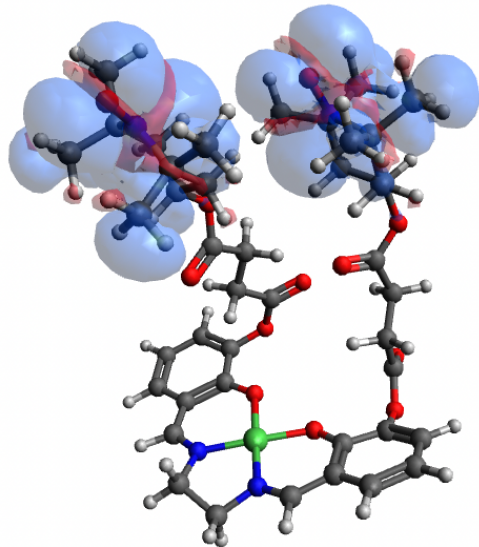


Figure 2.2: DFT on DiTS

polymer fragments under external electric field. The molecular systems for electrochemical charge storage are inherently disordered materials and the electric performance of a film containing those molecules is strongly dependent on the deposition method, as well as on the molecular structure See [77] (!). Therefore, so far there has not been a unified physical model that would describe the charge transport phenomena in such materials. The particular charge transport models have been developed that are applicable to certain classes of polymers (read that chapter in the polymer book and show what was done).

Chapter 3

Operando EPR Spectroscopy of TEMPO-Salen Electrochemical Cells

3.1 Electron Paramagnetic Resonance

In this section, the phenomenon of electron paramagnetic resonance is briefly described with details that are required to interpret the spectra of a charging electrochemical cell containing nitroxide radicals attached to a conjugated polymer backbone. After the introduction of the spin Hamiltonian, an experimental procedure to observe the corresponding spin transitions with continuous microwaves is described. The characteristic spectra of nitroxide radicals in various environments are described. That information is used to decompose the complex spectra of a charging cell to identify the state of charge of the cell and the by-products that are being released during the cell operation.

3.1.1 The Spin Hamiltonian

Electron Spin In the Poincaré group of special relativity [59], when rotations are considered together with the relativistic boosts [13], there emerges an additional quantity that is associated with rotation and is preserved together with the orbital angular momentum, yet this quantity is retained for point objects - it is called spin [36]. Spin is quantized [20]; it can take values in integer- or half-integer multiples of the Planck's quantum of action \hbar up to a certain magnitude S . The electron, as a fundamental particle and a fermion, bears a half-integer spin with a magnitude $S = 1/2$.

An isolated electron has two degenerate spin states - spin-up $|\uparrow\rangle$ and spin-down $|\downarrow\rangle$ - that are eigenfunctions of the square of the spin operator \hat{s}^2 with the same (degenerate) eigenvalue $\hat{s}^2|\uparrow\rangle = \hat{s}^2|\downarrow\rangle = \frac{3}{4}\hbar^2$. The states $|\uparrow\rangle$ and $|\downarrow\rangle$ are also eigenfunctions of the z

component of the spin operator, but correspond to different (non-degenerate) eigenvalues $m_s = \pm \hbar/2$ [?]:

$$\begin{aligned}\hat{s}_z |\uparrow\rangle &= +\frac{\hbar}{2} |\uparrow\rangle \\ \hat{s}_z |\downarrow\rangle &= -\frac{\hbar}{2} |\downarrow\rangle\end{aligned}\quad (3.1)$$

g factor Spin combines with the charge of the electron to endow the electron with a magnetic moment $\mu_{spin} = \gamma S$, where $\gamma = \frac{g_e \mu_B}{\hbar} \approx 28$ GHz/T is the gyromagnetic ratio of the electron, $\mu_B = \hbar e/m_e$ is the Bohr magneton and $g_e \approx 2$ is the electron g factor [5]. The g factor connects the spin of a particle with a magnetic moment that the particle expresses through interactions with external fields [67]. The Dirac quantum theory of the electron predicts $g_e = 2$ [57]. However, up to date, $g_e = 2.00231930436256(35)$ has been measured to the unprecedented accuracy of 0.13 ppt [14]. This measurement lies at the frontier of modern particle physics and the accordance of the measured g_e with the value obtained with quantum electrodynamics [67, 14] is the triumph of the quantum field theory [16].

Depending on the local environment of an electron, its g factor can change from g_e due to the spin-orbit coupling that changes the observed magnetic moment of the electron [5]. The magnetic moment of an electron can therefore be used as an extremely sensitive probe of the electron's local environment. The g factor of an electron localized in a molecular orbital can be anisotropic, depending on the shape of the orbital. Anisotropic g factor is represented by a 3×3 g matrix that can almost always be diagonalized [5] by an appropriate rotation of the molecular coordinate system.

Zeeman Splitting When an electron is placed in a static magnetic field $\vec{B}_0 = B_0 \vec{e}_z$, its magnetic moment experiences a torque and precesses in the xy plane about the field axis with the Larmor frequency $\omega_L = \gamma B_0$. The magnetic moment of the electron has two possible projections on the magnetic field axis, according to 3.1. The two corresponding eigenvalues $\pm \frac{\hbar}{2}$ define the energy difference between the states $|\uparrow\rangle$ and $|\downarrow\rangle$ when the spin couples to the external magnetic field, that is known as the Zeeman splitting. The energy difference between $|\downarrow\rangle$ and $|\uparrow\rangle$ in a magnetic field is the Zeeman energy.

The energy of an isolated electron placed in the external magnetic field \vec{B}_0 is the energy of the electron's magnetic moment in that field, that is given by the eigenvalue of the spin Zeeman Hamiltonian: $\hat{H}_{EZ} = \frac{\mu_B}{\hbar} \vec{B}_0 g_e \vec{s}$. In the laboratory frame of reference $\vec{B}_0 \parallel \vec{e}_z$, $[\hat{H}_{EZ}, \hat{s}_z] = 0$, so \hat{H}_{EZ} and \hat{s}_z share the two eigenfunctions $|\uparrow\rangle$ and $|\downarrow\rangle$. The energies of the corresponding states are $E_{EZ}^{\pm} = \pm \frac{1}{2} \mu_B g B_0$ (see Figure 3.1), and their difference is the Zeeman splitting:

$$\Delta E_{EZ} = \mu_B g_e B_0 \quad (3.2)$$

The measurement of the magnetic moment of an electron can be done by measuring its Zeeman energy. The local molecular environment affects the electron's magnetic moment through spin-orbit coupling which can be seen as a deviation in the electron's g factor [5].

Nuclear Spin and Nuclear Zeeman Splitting A proton has a half-integer spin $S = 1/2$ that results in a magnetic moment $\mu_p = \mu_e \frac{m_e}{m_p}$, that is $\frac{m_p}{m_e} \approx 1836$ times smaller than the electron's magnetic moment. A neutron bears no charge but also has a half-integer spin $S = 1/2$. An atomic nucleus that consists of protons and neutrons has a magnetic moment which is a vector sum of the aligned spins of its protons and neutrons. The spin of a nucleus is defined by the arrangement of its nucleons and by the nuclear charge. A nitrogen nucleus has 7 protons and 7 neutrons that total in a nuclear spin $I = 1$ which, with the g factor for the nitrogen nucleus g_N , results in the nuclear magnetic moment of $\mu_N = \mu_B \frac{m_e}{m_N} g_N I$ that splits into three Zeeman levels corresponding to the three possible projections of the nuclear spin on the magnetic field axis, $m_I = -1, 0, +1$, analogously to the electron with $m_S = 1/2, -1/2$. The nuclear Zeeman splitting is more than two orders of magnitude weaker than the electron Zeeman splitting because of the difference in the masses of the particles.

Hyperfine Interaction The magnetic moments of an electron and a magnetic nucleus, such as nitrogen, couple in the hyperfine interaction: $H_{HF} = \vec{s}\mathbf{A}\vec{I} = H_F + H_{DD}$ with the hyperfine coupling tensor \mathbf{A} . The isotropic part $H_F = a_{iso}\vec{s}\vec{I}$, or the Fermi contact interaction, scales with the probability density of the electron at the position of the nucleus $a_{iso} = \frac{2\mu_0}{3\hbar} g_e \mu_e g_n \mu_n |\psi(0)|^2$ [65]. The anisotropic part $H_{DD} = \vec{s}\mathbf{T}\vec{I}$ with the dipolar coupling tensor \mathbf{T} takes into account the anisotropic magnetic dipole coupling between the magnetic moments of the electron and the nucleus. \mathbf{T} depends on the shape of the electron orbital, its 3×3 Cartesian matrix representation depends on the molecular frame of reference and can be diagonalized by rotating the coordinate system. The matrix representation of the hyperfine coupling tensor \mathbf{A} can be written as the sum of its isotropic and anisotropic parts: $\mathbf{A} = a_{iso}\mathbf{1}_3 + \mathbf{T}$ [75]. In its diagonal matrix representation \mathbf{A} reduces to its three principal components $[A_{xx}, A_{yy}, A_{zz}]$. The values of \mathbf{A} are typically given in MHz.

Exchange Interaction In a system of closely placed electrons, such as in a film of densely packed radicals, the electron orbitals may overlap significantly and the radicals may exchange electrons. The energy required to exchange the electrons is called the exchange coupling $H_{exch} = \vec{s}_1\mathbf{J}\vec{s}_2$, that becomes considerably large at inter-spin distances

below $r < 1.5$ nm or with a large spin delocalisation [66]. The positive \mathbf{J} corresponds to a weak coupling between s_1 and s_2 which leads to an antiferromagnetic or antiparallel alignment of spins with a total $S = 0$, whereas the negative \mathbf{J} causes the strong inter-spin coupling which leads to a ferromagnetic alignment with $S = 1$.

Nuclear Quadrupole Moment The nitrogen nucleus has a spin greater than 1/2 which alters the charge distribution within the nucleus which gives rise to a non-vanishing nuclear electrical quadrupole moment Q [66]. The interaction between the asymmetrically distributed charge and the gradient of the electric field at the nucleus is given by the nuclear quadrupole Hamiltonian $H_{NQ} = \vec{I}\vec{\mathbf{P}}\vec{I}$ with the nuclear quadrupole tensor \mathbf{P} that describes the coupling of the nuclear quadrupole moment to the electric field gradient.

The Spin Hamiltonian For the interactions considered in this thesis, the following Hamiltonian will be applied to describe the interactions of unpaired electron spins with their local environments, ranging by their magnitude:

$$H = H_{EZ} + H_{HF} + H_J + H_{NZ} + H_{NQ} \quad (3.3)$$

The electron Zeeman term H_{EZ} defines the requirements on the hardware and sets the range of the magnetic fields used in the spectroscopic experiments. The hyperfine interaction term H_{HF} allows for reconstruction of the hyperfine coupling tensor from the recorded spectra which is used as a marker to identify the molecular structure and dynamics of the mobile molecular fragments that are released during the operation of an electrochemical cell. The exchange interaction term H_J scales with the concentration of the electrons, so the information about \mathbf{J} can be used to characterize the packing of the molecular fragments in the electrode. The nuclear quadrupole interaction term may lead to spectral distortions in a highly charged cathode where electric fields may be sufficiently strong to introduce noticeable nuclear quadrupole couplings to the nitrogen nuclei.

3.1.2 cwEPR spectroscopy

First observed in 1944 [81, 80, 64], the phenomenon of electron paramagnetic resonance had quickly become a tool for probing local molecular environments in species that contain unpaired electron spins. A free electron, that does not interact with its environment and has $g = g_e$, experiences a Zeeman splitting of $\Delta E = g\mu_B B_0$, that corresponds to the energy of a photon with a frequency of $\nu = \Delta E/h$. A microwave photon can drive a magnetic dipole transition between the Zeeman-split spin states - this is called electron paramagnetic resonance (EPR). An X band microwave photon (IEEE X band, $\nu = 8 - 12$ GHz, $\lambda = 2.5 - 3$ cm $^{-1}$)

3.8 cm, Figure 3.1, left) can drive the magnetic dipole transition between $|\uparrow\rangle$ and $|\downarrow\rangle$ at $B_0 \approx 0.3$ T. In a continuous-wave electron paramagnetic resonance (cwEPR) experiment, the microwave frequency and power is kept constant while B_0 is scanned and the microwave absorption is observed. EPR happens around the B_0 values given by the spin resonance condition:

$$\mu_B g_e B_0 = h\nu \quad (3.4)$$

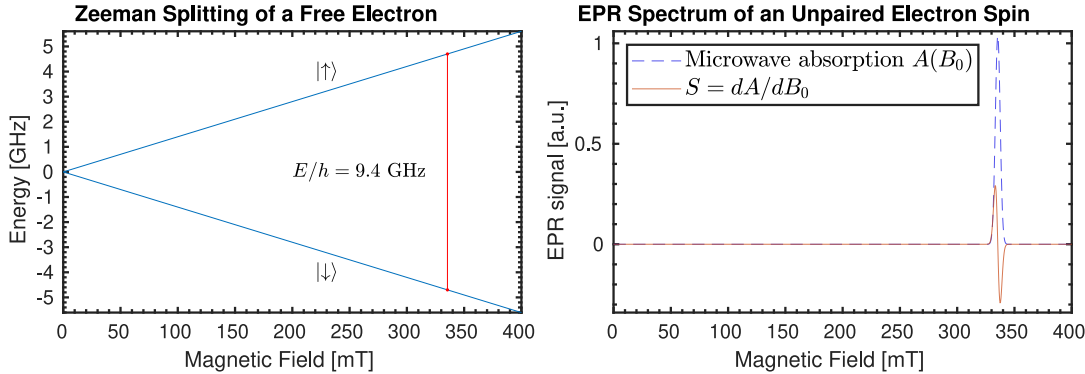


Figure 3.1: Left: Zeeman splitting for the energies of the two states of an isolated electron spin in a static magnetic field computed with EasySpin [?]. Vertical line is the magnetic dipole transition driven by a 9.4 GHz microwave photon. Right: Microwave absorption and its derivative as a function of the static magnetic field for an unpaired electron spin with a 5 mT Gaussian broadening to show the realistic shape of the cwEPR spectrum.

When B_0 reaches the value that satisfies Eq. 3.4, the sample starts absorbing microwaves. The absorbed microwave power recorded as a function of B_0 is the cwEPR spectrum (Figure 3.1, right, dashed). By construction, cwEPR spectrometers typically record the derivative of the microwave absorption vs. B_0 (Figure 3.1, right, solid). Advanced spin resonance techniques methods that involve coherent spin dynamics and pulsed microwave fields are discussed in Chapter 4.

Line Broadening "EPR spectra do not consist of a discrete set of infinitely sharp lines. Lines are broadened by dynamic effects (relaxation, tumbling, chemical exchange) or static effects (orientational disorder, unresolved hyperfine splittings, distributions in magnetic properties such as g , A , and D values)."

cwEPR spectrometer A basic cwEPR spectrometer consists of a magnet, a microwave source, a resonator and a microwave detector. Figure 3.2 depicts those elements with more

details, including the sample - an electrochemical cell that is placed inside the microwave resonator and its SoC controlled with an external potentiostat.

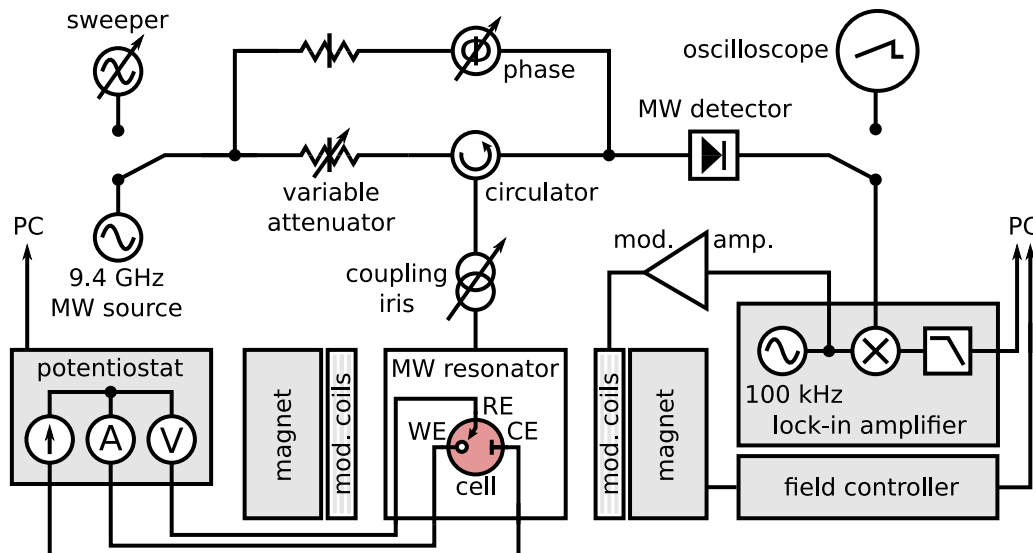


Figure 3.2: Diagram of a cwEPR spectrometer

Continuous microwaves are generated with a klystron (MW source in Figure 3.2) and directed towards the resonator (resonating cavity) through the signal arm that contains a variable attenuator and a circulator. The circulator directs the microwaves from the source to the cavity and passes the microwaves reflected from the cavity further to the microwave detector. The adjustable coupling iris between the circulator and the resonating cavity allows one to match the impedance of the cavity to the impedance of the signal arm so that minimal microwave power is reflected back from the cavity at a non-resonant field B_0 . That impedance matching is called critical coupling. At the microwave detector, the microwaves reflected from the cavity are compensated by the microwaves with fixed microwave power and an adjustable phase, that pass through the reference arm. The signals from the two arms interfere destructively at the detector, so that there is no signal at the detector for non-resonant B_0 .

When the resonance condition (Eq. 3.4) is met, the incident microwaves are being absorbed by the sample and the resonator's Q factor slightly changes. The change in the Q factor decouples the resonator from the signal arm, that causes additional reflections in the signal arm. The microwaves in the signal arm that are not compensated by the reference arm become detected by the microwave detector - a biased semiconductor diode that has a linearly changing conductivity in the range corresponding to the incident microwave power. A phase sensitive detection with shallow modulation of B_0 increases the signal-to-

noise ratio (SNR) and yields the derivative of the microwave absorption profile vs. B_0 . The typically high $Q \gg 1$ factor of the resonator further increases the SNR, as the decoupling of a resonator with higher Q leads to a larger reflected microwave power.

To ensure that only the magnetic component of the microwave is interacting with the sample, a standing microwave is formed in the resonating cavity. In the center of the cavity, the magnetic component of the microwave is maximized and the electric component is quenched. When a small sample is inserted in the center of the cavity, it is mostly the magnetic component of the microwave that is interacting with it. That allows one to drive magnetic dipole transitions without heating up the sample by the electric component. For larger samples as, for example, working electrochemical cells, the separation between the electric and magnetic microwave components does not hold within the full sample volume. Furthermore, the insertion of a cell containing metal electrodes and polar electrolyte into a resonator changes the distribution of the microwave field in it and lead to a non-resonant microwave absorption.

3.2 cwEPR Spectroscopy of TEMPO Containing Molecular Fragments

The stable TEMPO[•] radical is widely used in the EPR spectroscopy as a spin probe and particularly in the EPR studies of TEMPO containing ORB materials [50, 53, 2, 1, 32, 85]. The spin density at the TEMPO[•] radical is localized within the N-O bond [56] and partially resides on the $I = 1^{14}\text{N}$ nucleus, so to describe the EPR spectrum of an isolated TEMPO[•] one has to take into consideration the electron Zeeman term H_{EZ} , the nuclear Zeeman term H_{NZ} and the hyperfine coupling term H_{HF} . The unpaired electron spin on TEMPO[•] has anisotropic g value, because of the asymmetry of its molecular orbital, so the \mathbf{g} matrix and the \mathbf{A} hyperfine coupling tensor are both anisotropic. \mathbf{g} is diagonal in the molecular frame of reference shown in Figure ???. Its principal values are $[g_{xx} = 2.009, g_{yy} = 2.006, g_{zz} = 2.002]$ [43, 4]. The principal values of \mathbf{A} in the same frame are $[A_{xx} = 0.0000, A_{yy} = 0.0000, A_{zz} = 0.0000]$ MHz [43, 4].

3.2.1 Room Temperature Spectra of TEMPO[•] Solutions

Solution spectra of radicals are showing averaged values of g and A because of the fast molecular tumbling [43, 6]. The observed g value for a tumbling TEMPO[•] is the average of the principal values of the \mathbf{g} matrix: $g = 1/3(g_{xx} + g_{yy} + g_{zz})$. The anisotropic part of the hyperfine coupling tensor for the tumbling TEMPO[•] also averages to zero, so only the isotropic hyperfine constant a_{iso} determines the observed hyperfine coupling. CwEPR

spectra of a 0.1 mM solution of TEMPOL measured at room temperature are shown in Figure ???. The spectral simulation performed with EasySpin [?] yields $g = 2.0055$ and $a_{iso} = 43.8$ MHz.

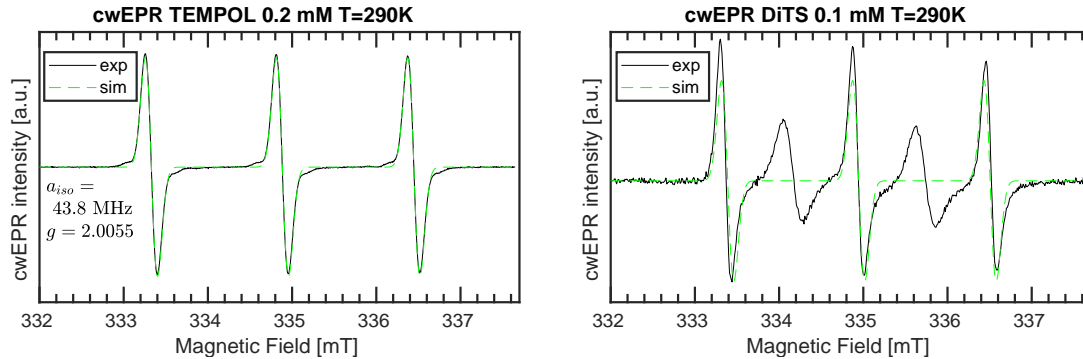


Figure 3.3: Room temperature cwEPR spectra of a low-concentration solutions containing mono- and di-TEMPO molecular fragments. Left: TEMPOL, Right: Di-Tempo-Salen.

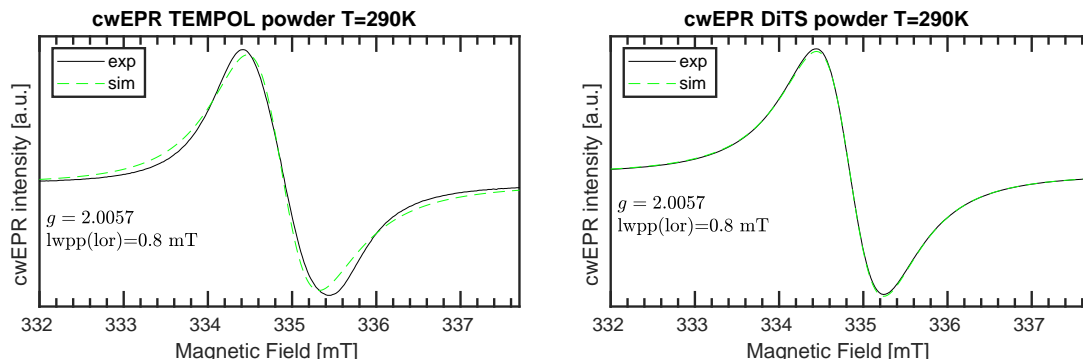


Figure 3.4: Room temperature cwEPR spectra of pure TEMPO-containing powders. Left: TEMPOL, Right: Di-Tempo-Salen.

A biradical molecule like Di-Tempo-Salen (Figure ??,x) has two paramagnetic species that are close to each other and therefore exchange electrons. When the exchange coupling between the radicals J is comparable to the hyperfine coupling A of each radical to its 'host' nucleus, the superhyperfine interaction [] takes place, in which the radical is interacting to the nucleus of the neighboring radical [?]. Solutions of biradical molecules with magnetic nuclei show more features in cwEPR spectra when the electron-electron exchange coupling J between the two radicals within the molecule becomes comparable to the hyperfine coupling between the radical and its 'host' ^{14}N nucleus. tumbling of the

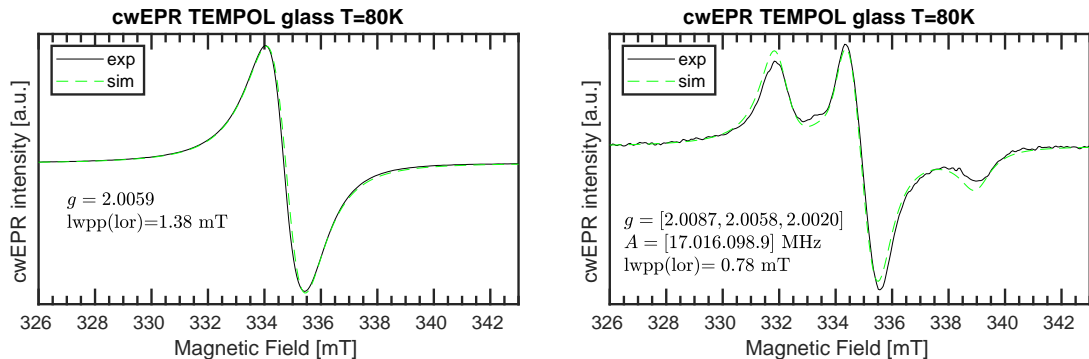


Figure 3.5: Cryogenic cwEPR spectra of TEMPOL at high and low concentration in a Dichloroethane/Acetonitrile glass. Left: 100 mM, Right: 0.1 mM.

molecule and the restricted motions of each radical within the molecule cause a complex molecular motion that affects the dipolar and exchange couplings between the radicals and causes "spectra with alternating linewidths" [?, ?]. A solution of Di-TEMPO-Salen shows a five-line cwEPR spectrum with alternating linewidths (Figure ??, right) with the three most intense lines corresponding to the three hyperfine sublevels of TEMPO^{\bullet} . The five-line structure in the cwEPR spectrum indicates the presence of a di-TEMPO biradical in the solution.

TOLYAN:

If the TEMPO groups are far away from each other, their cw-EPR signal consists of three lines that are due to the hyperfine interaction between the electron spin and the spin of the Nitrogen nucleus. When the TEMPO groups are brought closer to each other, their electron orbitals start to overlap, and the exchange interaction (J) between the electrons grows. That splits the signal into more lines as it was shown by [10] and represented in Fig. 7. In the case of strong exchange interaction the spectrum consists of five lines with relative ratios 1:2:3:2:1. In the absence of the exchange interaction the spectrum contains only three hyperfine lines of equal intensities. In DiTS, a sum of a three-line spectrum and a five-line spectrum was observed. This may be the evidence that TEMPO-bearing linkers are sufficiently long to allow TEMPO groups to move freely in space around the organometallic complex. That can yield to different J values depending on the relative orientation of the linkers, similar to [10]. In theory, there are several possible positions of TEMPO groups relative to each other that can change the EPR spectrum. Depending on the angle between the linkers (from π to 0), J may vary from its minimal to maximal value, that should yield a three- and five-line structures respectively. Since the process of movement is dynamic, we can explain the observed picture as a combination of several positions in space [10]. The five-line structure suggests different preferred conformations

of the TEMPO fragments and dynamic interconversion between these states with different exchange coupling J leads to the observed spectrum.

3.2.2 Spectra of TEMPO $^{\bullet}$ /TEMPO $^{+}$ Films

A film made of a TEMPO-containing polymer can be brought to a certain oxidation state, depending on how many of the TEMPO groups are in the radical (TEMPO $^{\bullet}$) state and how many are in the oxidized (TEMPO $^{+}$) state. The densely packed TEMPO $^{\bullet}$ fragments in the film cannot be considered as isolated molecules anymore, and the interactions between the radicals become significant. Microcrystals of TEMPOL are densely packed TEMPO $^{\bullet}$ with a concentration of ??? mM. The cwEPR spectrum of TEMPOL in Figure ?? is one broad line centered at $g = 2.0055$.

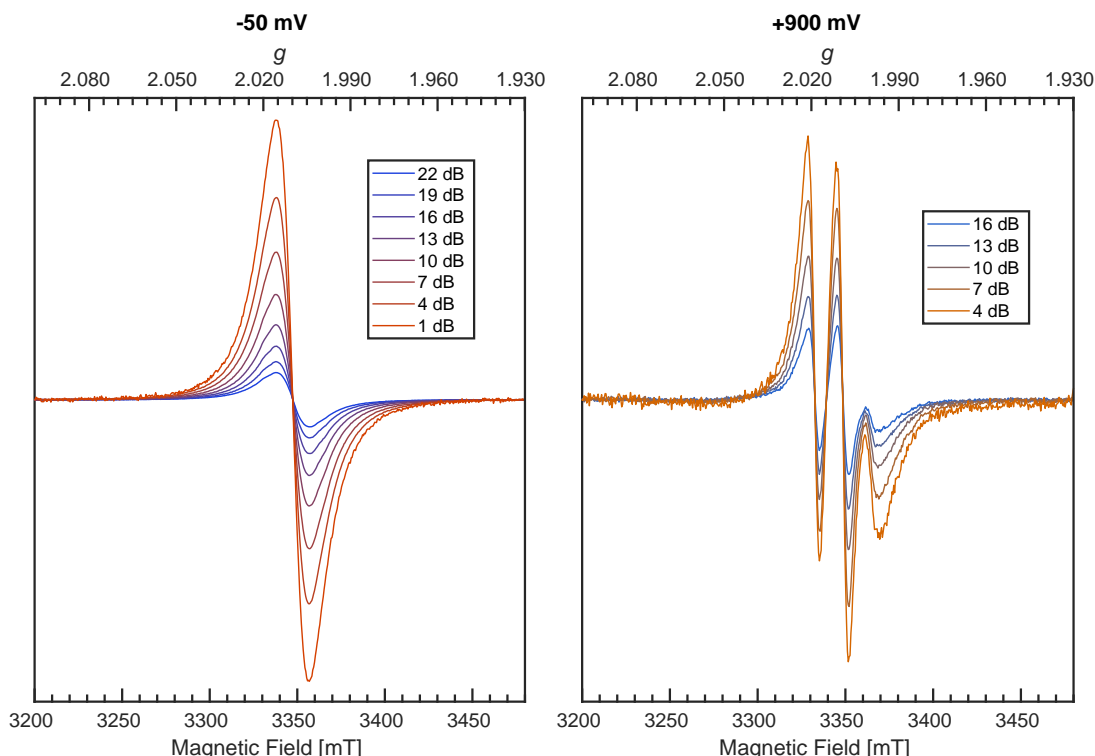


Figure 3.6: Cryogenic (80 K) cwEPR spectra of a pDiTBuS film grown with 200 deposition cycles. Left: discharged film, -50 mV vs. Ag/AgNO₃ RE. Right: Fully charged film, 900 mV vs. Ag/AgNO₃ RE.

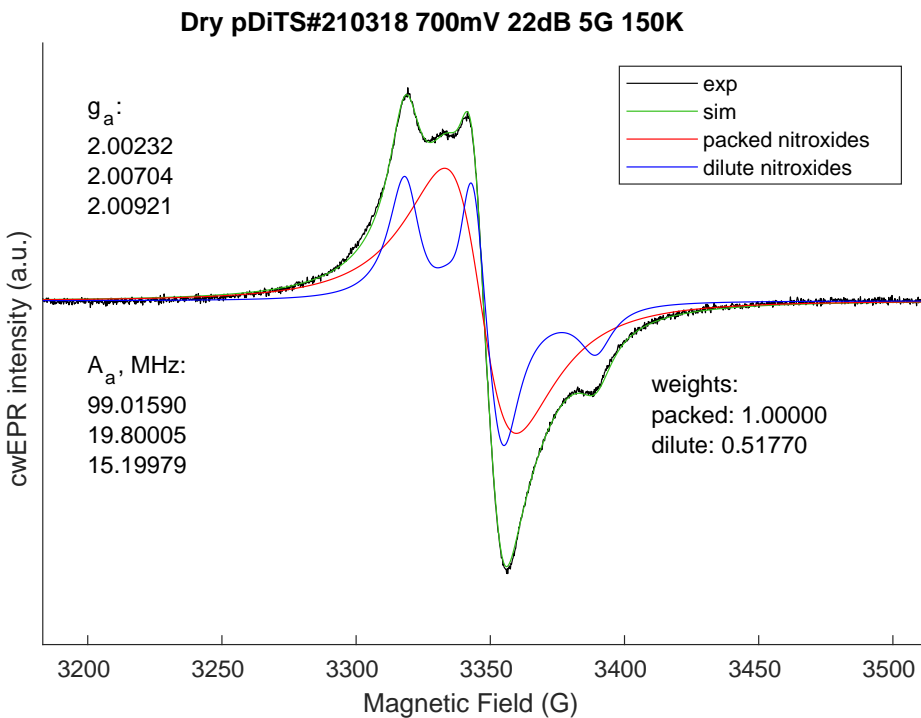


Figure 3.7: A pDiTS film in the intermediate state of charge (700 mV vs. Ag/AgNO₃) showing a composition of two spectral signatures. The single-line signal from the densely packed nitroxide radicals coexists with the signal of the isolated nitroxide radicals. Two-component simulation.

3.2.3 Spectra of NiSalen Films

3.3 cwEPR Spectroscopy of a Charging Electrochemical Cell

There is a number of difficulties when it comes to an EPR experiment on a working electrochemical cell. The cell must contain mobile ions between its electrodes - cations and anions. The ions are normally produced as products of dissociating salts. To overcome the ionic bond in a salt and to break it into the ions, a solvent with large dipole moment is needed. Solvents with large dipole moments, as acetonitrile (CH₃CN, $\epsilon \approx 37.5$) or water ($\epsilon \approx 78.4$), have large dielectric constants which results in a non-resonant absorption of microwaves. A cell containing liquid electrolyte absorbs microwaves and lowers the sen-

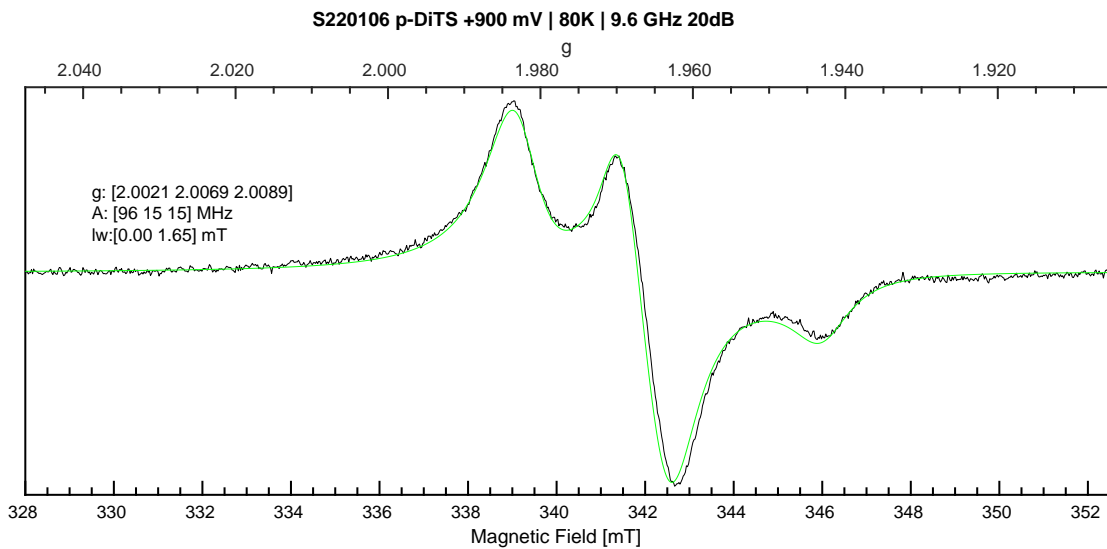


Figure 3.8: Simulation of the cryogenic (80 K) cwEPR spectrum of an oxidized pDiTBuS film grown with 200 deposition cycles showing a signature of the isolated nitroxide radical with $g = ?$ and $A = ?$.

sitivity of the EPR experiment. Furthermore, due to a finite dimension of cell, not only the magnetic component of the microwave is interacting with the electrolyte, but also the electric one - this results in heating of the electrolyte in a similar fashion as in a microwave oven. The heating of the electrolyte leads to a faster degradation of the cell and does not allow for long systematic measurements.

Another general issue with the operando EPR and EDMR experiments is that the device under testing (DUT) has to have metal electrodes that deliver current to it. Metals, placed in a microwave cavity, change the distribution of the electromagnetic field in it - that weakens the magnetic component at the device and at the same time strengthens the electric component. It is the magnetic dipole transition that is causing the magnetic resonance, so the weakening of the magnetic component by introducing the metal electrodes further decreases the magnetic resonance response. The increased electric component causes heating to temperatures that can be critical for the DUT operation.

3.3.1 Fabrication of EPR-compatible Electrochemical Cells

3.4 Versatile electrode setup for ex-situ and in-situ spectroelectrochemical EPR

There is increasing interest in both ex-situ and in-situ spectroelectrochemical (SEC) EPR measurements in research fields ranging from biology to materials science, from redox active systems such as proteins [?] and hydrogenase to catalysis,[?, ?, ?, ?, ?] redox-flow batteries [?] and of course ORBs.[26, ?] One significant drawback with SEC EPR is the fact that microwave resonators suffer from substantial microwave damping as a result of introducing metal electrodes, polar solvents and ionic salts (i.e., the electrolyte) needed for successful electrochemistry.[?] Microwave damping can be significantly reduced by our novel on-substrate electrode design (see Fig. 3.11) as this limits the amount of metal that is introduced into the resonator, while still allowing us to have electrode surface areas large enough to deposit sufficient material of interest to observe EPR signals.

The on-substrate electrodes are produced as follows. Cleaned quartz substrates are placed inside a holder and covered with shadow masks. The assembly is transferred into a vacuum chamber equipped with a thermal evaporator (MBraun ProVap 5G PVD System). At a pressure of 7×10^{-7} mbar, 10 nm of Chromium (Cr) adhesion layer is evaporated, followed by 180 nm of Gold (Au). In this way the on-substrate working and counter electrodes are formed (WE and CE respectively). The reference electrode (RE) is not evaporated on substrate for electrochemical stability reasons. Instead, a 250 μm Ag wire is used, either as is or, for additional stability, coated galvanically with a AgCl layer.[?] See Section ?? in the ESI† for details of the sample preparation.

The above procedure provides a WE active area of 12.0 mm^2 which allows one to deposit an electrochemically active film that is large enough to yield a clear EPR signal. The flat electrode design provides the possibility to increase the WE area for samples with particularly small EPR signals while still maintaining certain film thicknesses. This also allows for studying EPR properties as a function of film thickness. In cases where the electrochemical process is thought to deposit material on both the WE and CE, the distance between the on-substrate electrodes can be adjusted such that only one of the electrodes is positioned in the active volume of the microwave resonator, allowing for selective EPR probing of either of the electrodes.

The on-substrate electrodes reduce microwave damping. However, a substantial amount of microwave damping occurs due to the electrolyte, made of polar solvent and ionic salts. Therefore, we further optimize our setup by modifying conventional 5 mm outer diameter (OD) quartz EPR tubes by flattening the bottom 1.3–1.6 cm (cf. Fig. 3.11b and Section 3.12 in the ESI†), thereby reducing the active electrolyte volume needed to submerge both

the WE and CE on the substrate as well as the RE wire, from $\sim 120 \mu\text{L}$ to $\sim 60-70 \mu\text{L}$.

The flattened tube and the thin-film electrode setup have an additional benefit in that the sample is moved away from the maximum of the electric field distribution in the Bruker ER 4122-SHQE resonator (TE_{011} mode cavity for cwEPR), thereby further increasing the resonator quality factor (Q-factor, given by $Q = \frac{\nu_{res}}{\Delta\nu}$, ν_{res} = resonance frequency, $\Delta\nu$ = FWHM of the resonance dip) and hence sensitivity. Further improvements can be made using the flat electrode setup in a TM_{110} mode cwEPR cylindrical cavity such as a Bruker ER 4103-TM (developed for studying samples exhibiting high dielectric constants), where the flattened cell can be aligned to further reduce coupling to the microwave electric field. The modified tube is compatible with commercial Bruker ER 4118X-MD5 resonators, most commonly used for advanced pulse EPR measurements at X-band frequencies ($\nu = 9 - 10 \text{ GHz}$).

3.4.1 Fabrication of the modified tube

The volume of the cell used in this study had to be minimized, as the high dielectric constant of the electrolyte does not allow for the critical coupling of the resonator. The volume of the electrolyte was minimized by flattening the tip of the quartz (melting point $T_m = 1660-1710^\circ\text{C}$) tube accommodating the cell. For that, a tungsten (W, $T_m = 3420^\circ\text{C}$) rod of a $3.70 \times 1.35 \text{ mm}$ rectangular cross section, narrowing to the bottom of the tube at a wedge angle of $\alpha \approx 5^\circ$, was inserted into the tube (Fig. 3.12). The tube was evacuated and filled with He to a pressure of 100 mbar. The tip of the evacuated tube was molten around the thermally expanded rod with a Hydrogen-Oxygen burner ($T_f = 3080^\circ\text{C}$). The modified tube was then connected to atmosphere and the cooled, contracted rod was removed and later reused for modifying other tubes. The tungsten rod was fabricated from an electrode of a flash lamp of a pulsed Nd:YAG laser.

The modification of the tip of the tube provided a decrease in the volume of the electrolyte down to $45 \mu\text{L}$, while the cylindrical part of the tube allowed for fitting the substrate connector and the wiring in. That allowed for the room temperature EPR measurements on the electrochemical cell during charging and discharging. Extensive care had to be taken to reproduce the cv curve in the modified tube as the limited volume of the electrolyte was distributed over the large surface area. That caused poor ionic transport in the electrolyte layer.

To establish the extent to which the modified tube improves the resonator Q-factor (Q) and therefore sensitivity of the cwEPR experiment, cwEPR spectra and associated Q-factors were recorded for a flat-electrode p-DiTS cell assembled in two different sample

3.4. VERSATILE ELECTRODE SETUP FOR EX-SITU AND IN-SITU SPECTROELECTROCHEMICAL EPR

tubes. For both cell setups we used enough electrolyte to submerge all three electrodes. This required $100 \mu\text{L}$ for the standard tube and $70 \mu\text{L}$ for the modified tube. The effect of the two tubes on the cwEPR spectrum and on the Q-factor was studied for a range of heights (H) measured from the center of the microwave resonator to the middle of the WE.

3.4.2 Q-factors and cwEPR spectra for p-DiTS in standard and modified tube

We determine $Q \approx 7800$ for the empty resonator. Inserting the tube-based cells initially at $H = 24$ mm reduces the Q-factor for both cases, but more significantly for the standard tube ($Q_{\text{standard tube}} \approx 4200$, $Q_{\text{modified tube}} \approx 5400$, see Fig. 3.13). At $H = 18$ mm the Q-factor drops for both, again more significantly for the standard tube to $Q_{\text{standard tube}} \approx 300$ while for the modified tube it is still $Q_{\text{modified tube}} \approx 1200$, a factor of 4 difference. This difference between the two tubes shows the benefit of using the modified tube and flat electrode geometries for SEC EPR. When the modified tube is inserted as deep as $H = 14$ mm, the $Q_{\text{modified tube}}$ is around 400, which still allows for EPR measurements. Coupling the resonator not possible for $H < 18$ mm (standard tube) and $H < 14$ mm (modified tube).

The decreasing Q-factor is not the only effect of a high-dielectric sample in an EPR resonator. The interaction between the sample and the electric field distribution of the resonator causes a mixture of absorption and dispersion signals, leading to asymmetric lineshapes in the cwEPR spectra. This makes double integration of the derivative cwEPR signal more complex, thereby making a quantitative analysis more difficult. This effect can be seen in the cwEPR spectra of p-DiTS (Fig. 3.13) measured in the standard 5 mm tube for $H = 18$ mm where the cwEPR signal is asymmetric. The modified tube yields symmetric lineshapes at the same sample heights. Further details are presented in the following subsection.

The electrochemical cells based on the modified tube allow for higher EPR signals as compared to the normal X-band EPR tube. Fig. 3.14 represents two sets of measurements that describe the enhancement of the EPR signal for the modified tube. When the cell is inserted closer to the resonator's center, the Q factor of the resonator lowers and the EPR signal increases, because the intensity of the magnetic component of the microwave field B_1 is higher in the center of the resonator. When the cells were inserted closer to the center of the resonator, the Q factor went from ≈ 6000 down to ≈ 400 , so that the microwave bridge could not be critically coupled to the resonator and no EPR measurements were possible. Depending on the volume of the electrolyte in the cell, it can be inserted more or less deep into the resonator.

The modified tube could be inserted 7 mm deeper into the microwave resonator (see Fig. 3.14). The EPR signal in the modified tube is increased as compared to the normal

tube at the same height.

The modified tube also allows for larger cwEPR signal intensities as it can be inserted closer to the resonator center. The signal-to-noise ratio (S/N) for the modified tube is increased by a factor of ≈ 6 as compared to the standard tube, both inserted at $H = 18$ mm. At the maximum sample insertion, the S/N is improved by a factor of ≈ 8 for the modified tube.

Using the modified tube we see three major benefits. Firstly, it results in much higher Q-factors and therefore sensitivity when comparing Q-factors for the same sample height. Secondly, the modified tube allows for insertion of the tube closer to the resonator center, allowing for a larger S/N and therefore requiring less averaging time for each cwEPR measurement. This is especially useful for samples where holding the potential for long periods causes unwanted effects or degradation. Thirdly, cwEPR measurements with the modified tube give symmetric cwEPR lineshapes (using the conventional procedure for critically coupling the microwave cavity, the standard tube gives an asymmetric lineshape) which allows for more straightforward quantitative analysis (spin counting), especially useful for in-situ cwEPR with varying redox potentials.

3.4.3 cwEPR Spectra During a Charge-Discharge Cycle

There are four characteristic cwEPR signatures of an electrochemical cell containing di-TEMPO-Salen polymer cathode. The well known signature of a freely tumbling TEMPO \cdot exhibits three narrow lines corresponding to the three nuclear sublevels of nitrogen: $m_I = -1, 0, +1$.

EPR spectra of electrochemical cells with p-DiTS as active-electrode material can exhibit a variety of different signals. Before presenting and discussing the experimental results, we will provide an overview about the various characteristic cwEPR lineshapes associated with nitroxides in different environments.

Fig. 3.15a shows the spectrum expected for a *densely packed p-DiTS film* with all nitroxides in the EPR-active reduced state. The broad unstructured line results from the strong dipolar and exchange interaction between both nitroxides of each DiTS monomer as well as between the nitroxides of different monomers. The exchange interaction can lead to either line narrowing or broadening depending on the strength of the interaction,[?] while the dipolar interaction causes broadening. In consequence, the overall cwEPR line width depends on the spin concentration in the film.

Dilute mono-TEMPO fragments dissolved in the electrolyte, each containing only one nitroxide, give rise to a three-line spectrum (cf. Fig. 3.15b) which is well known from nitroxide-based spin labels in solution.[?] Tumbling of the molecules in the liquid electrolyte results in an averaging of the anisotropic interaction between the electron spin and

3.4. VERSATILE ELECTRODE SETUP FOR EX-SITU AND IN-SITU SPECTROELECTROCHEMICAL EPR

the nitrogen nuclear spin ($I = 1$) as well as of the g anisotropy, leaving only the isotropic part of the hyperfine coupling and the isotropic g value.

Dilute DiTS monomers in the electrolyte generally give a spectrum consisting of five narrow lines (cf. Fig. 3.15c), if each monomer contains two interacting EPR-active nitroxides. The spectrum depends on dynamic effects, specifically the modulation of the exchange interaction between both radicals of each monomer. Thus, depending on the solvent and temperature, the spectrum can be indistinguishable from the three-line spectrum of mono-TEMPO fragments.

The fully charged (oxidized) p-DiTS film can contain electrically isolated domains in which the nitroxides are not connected to the electrode and cannot be oxidized or reduced. These electrically inactive *immobilized DiTS monomers* in the oxidized film display a spectrum as shown in Fig. 3.15d. In contrast to the densely packed p-DiTS film, the dipolar and exchange interactions between neighboring radicals are much weaker. The anisotropy of the nitroxide's hyperfine tensor adds features to the cwEPR spectrum in d) as compared to a). Yet, there is some remaining line broadening that does not allow one to distinguish between immobilized DiTS monomers with either one or two paramagnetic nitroxides.

We note that the oxidized NiSalen backbone can contribute to the spectrum as well. Its EPR signature, which is not shown in Fig. 3.15, is clearly different from the nitroxide/TEMPO-related spectra discussed above.

3.4.4 Spectral Simulations

3.4.5 Quantitative Analysis of Potential-Dependent EPR Spectra

3.4.6 EPR-Detected State Of Charge

3.4.7 Formation of Singlet Spin States in a Reduced Cathode Film

3.4.8 Monitoring of Degradation Processes

The operando monitoring of EPR spectra in pDiTS cells has revealed that the amount of paramagnetic species reduces upon the cycling. The cwEPR spectra during one charge-discharge cycle of two different pDiTS cells are shown in Figure 3.19. Both datasets show a significant amount of the three-line structure in the oxidised (fully charged) state, that corresponds to the release of dilute nitroxide radicals from the polymer film to the electrolyte. The fact that the released species exhibit a 3-line structure and not a 5-line structure excludes the release of the di-TEMPO (DiTS) monomers and suggests that individual TEMPO[•] fragments are being detached from the film. Therefore, it was found that

it is the molecular degradation of DiTS that is responsible for the loss of cell's capacity and not the decomposition of the polymer film into the monomer fragments. The overall EPR signal intensity decreases for both samples after the charge-discharge cycle. The spectral deconvolution with quantitative analysis of the individual components has revealed that the released fragments do not explain the overall loss of the signal intensity after the cycle.

3.4.9 Monitoring of Self Discharge

Organic Radical Batteries have a tendency to self-discharge, as the organic electrochemically active layer partially dissolves in polar electrolytes. Particularly for the TEMPO containing ORB, the dissolved, mobile TEMPO fragments serve as redox shuttles that carry the charge between the battery electrodes and cause a self discharge. The amount of unoxidized TEMPO[•] shuttles can be measured with cwEPR spectroscopy as the mobile fragments have distinct spectra as compared to the fragments tightly packed in the electrode. Further in this subsection operando spectra of a TEMPO containing electrochemical cells are shown. Quantitative analysis of the released fragments during a charge-discharge cycle allows for a description of the self-discharge process in an ORB. The charge state of a battery is monitored with cwEPR and, additionally, with a potentiometric measurement to identify the self-discharge rate and to connect it with the concentration of diffusing redox shuttles.

3.4.10 Electrochemical Cells with Solid Electrolyte

3.4.11 Low Temperature Measurements

3.4. VERSATILE ELECTRODE SETUP FOR EX-SITU AND IN-SITU SPECTROELECTROCHEMICAL EPR

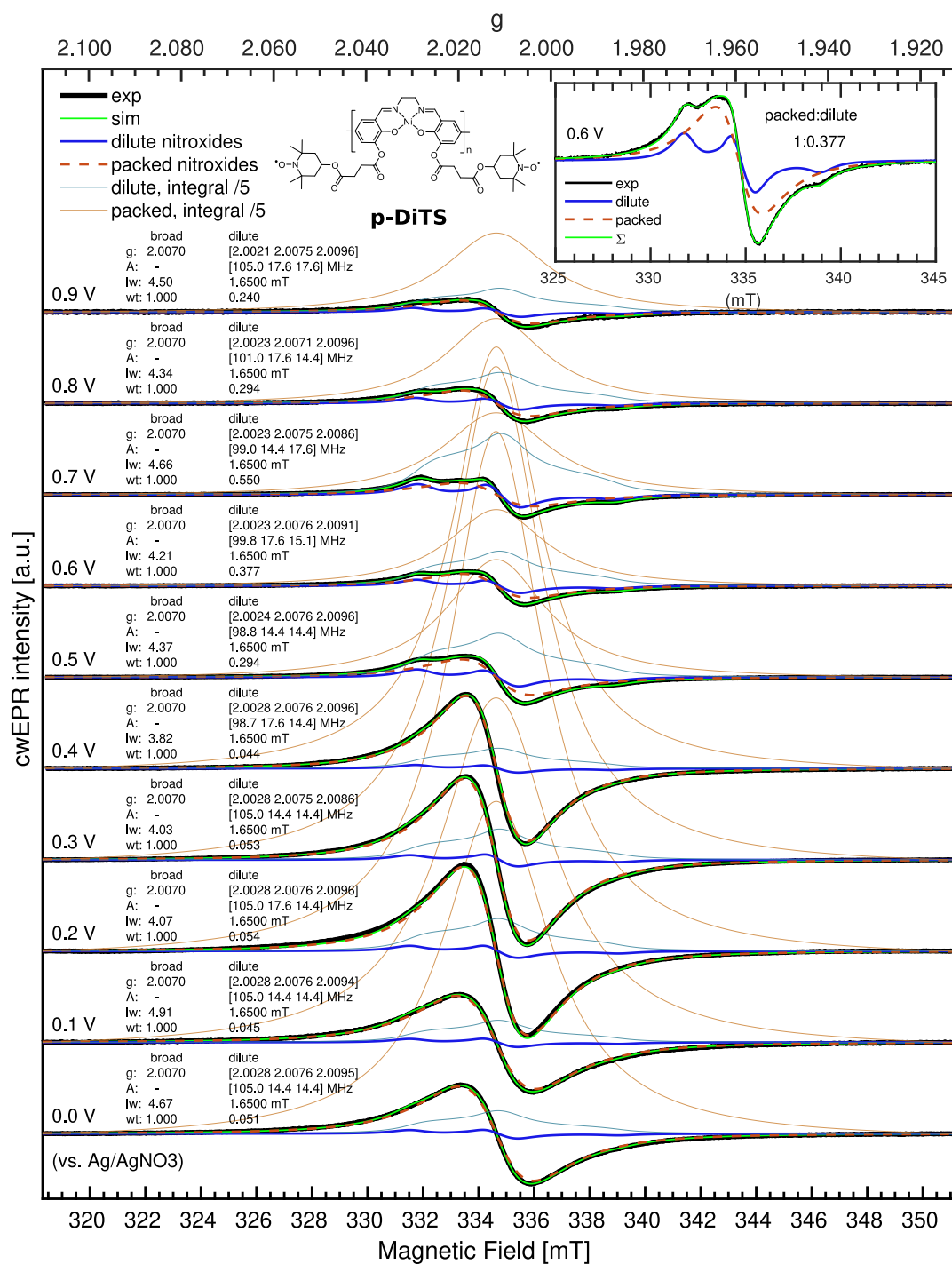


Figure 3.9: copy from SI.

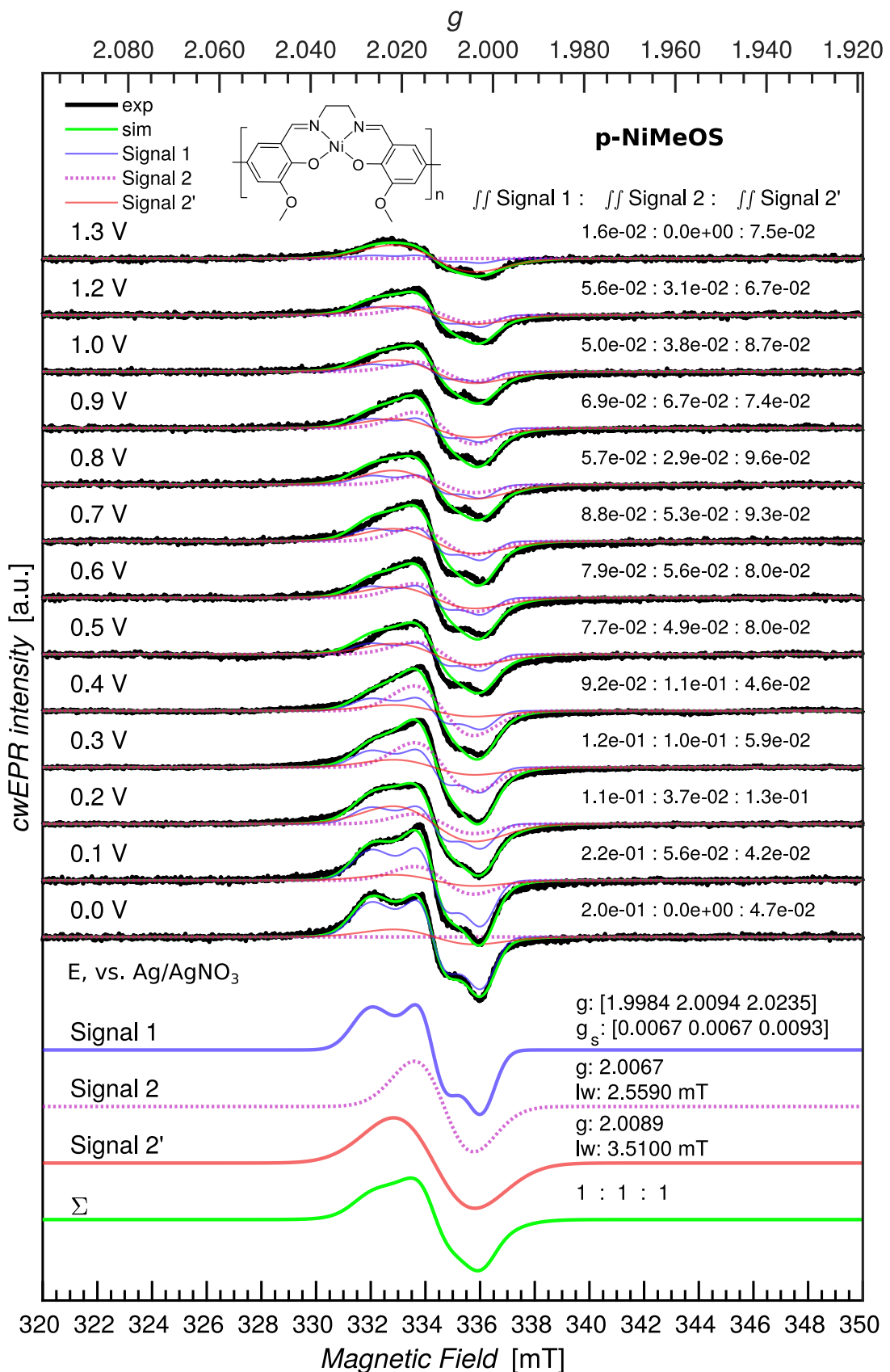


Figure 3.10: Potential-dependent cwEPR spectra of a NiMeOSalen film measured at 150 K. Simulation of the spectra with three components reported by the Timonov group.

3.4. VERSATILE ELECTRODE SETUP FOR EX-SITU AND IN-SITU SPECTROELECTROCHEMICAL EPR

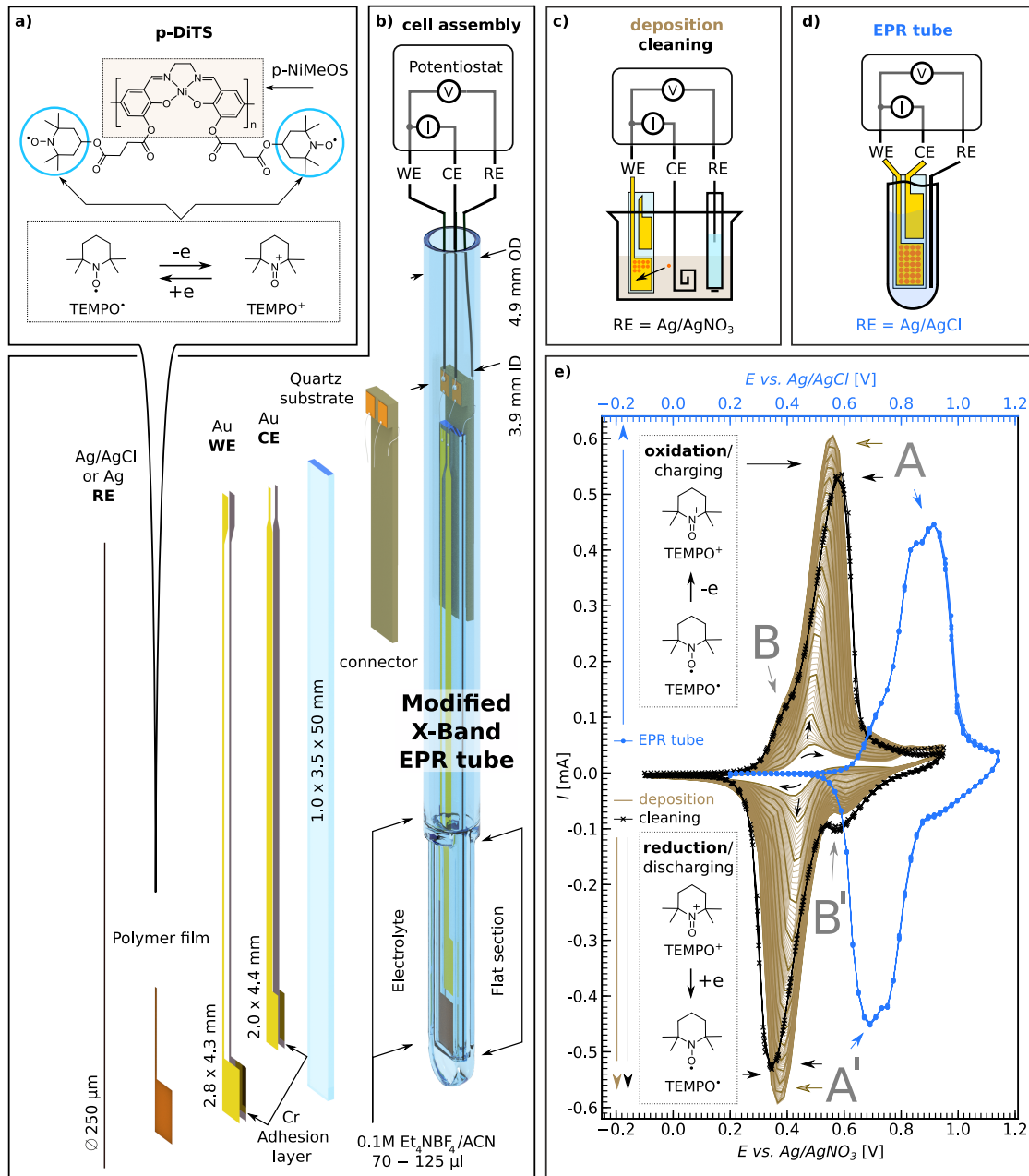


Figure 3.11: Schematic diagram of the electrode design and assembly of the electrochemical cell based on a modified X-band EPR quartz tube. a): Molecular structure of p-DiTS, with the redox reaction of its charge-bearing TEMPO groups; highlighted is the backbone, p-NiMeOSalen. b): Photograph of the modified tube with a flattened bottom section, with the on-substrate electrochemical setup assembled inside, and the process of forming the modified tube. c): Electrochemical setup for deposition and cleaning of polymer films. d): Tube-based electrochemical setup. e): Cyclic voltammograms of a growing p-DiTS film during 100 electropolymerization cycles (solid-brown), during the cleaning process (crossed-black) and in the tube-based setup (dotted-blue). Peaks A/A', B/B' correspond to the oxidation and reduction of the TEMPO fragments and of the p-NiSalen backbone, respectively. All CV were recorded at 50 mV s^{-1} .

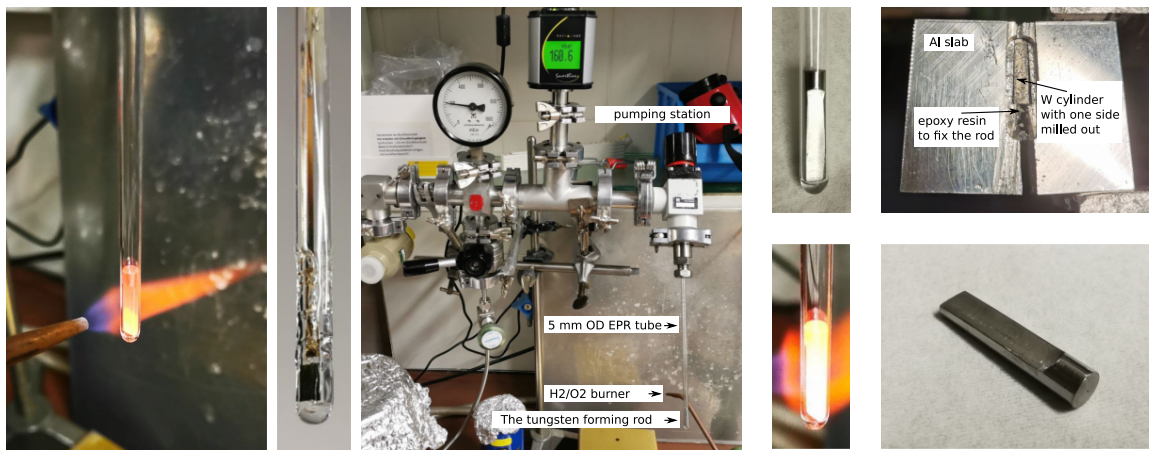


Figure 3.12: Modifying the tip of the standard 5 mm OD quartz EPR sample tube by melting it around a Tungsten (W) forming rod with a H₂/O₂ burner in an evacuation setup.

3.4. VERSATILE ELECTRODE SETUP FOR EX-SITU AND IN-SITU SPECTROELECTROCHEMICAL EPR

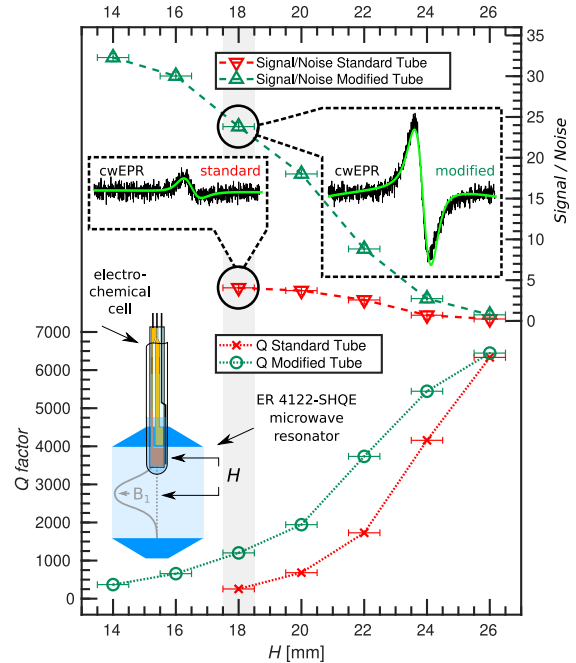


Figure 3.13: Signal-to-noise ratio of the cwEPR spectrum of p-DiTS and the Q-factor of the Bruker ER4122-SHQE microwave resonator measured for an electrochemical cell based on a standard X-band EPR sample tube and for an electrochemical cell based on the modified tube. Data for various heights H from the center of the resonator. Insets: Representative cwEPR spectra at $H = 18$ mm, where the signal for the standard tube is the strongest.

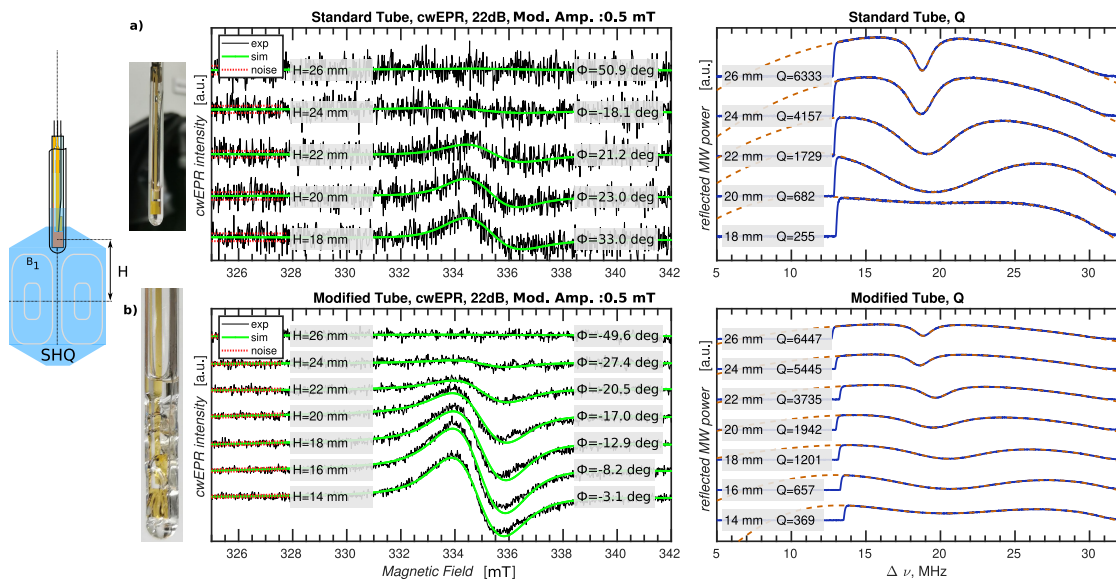


Figure 3.14: cwEPR signal intensity and Q factors for the standard 5 mm OD quartz EPR sample tube and for the modified tube at different heights from the center of the Bruker ER 4122-SHQE resonator. $\nu = 9.4$ GHz. Simulations of the cwEPR spectra with adjusted microwave phase. Noise analysis.

3.4. VERSATILE ELECTRODE SETUP FOR EX-SITU AND IN-SITU SPECTROELECTROCHEMICAL EPR

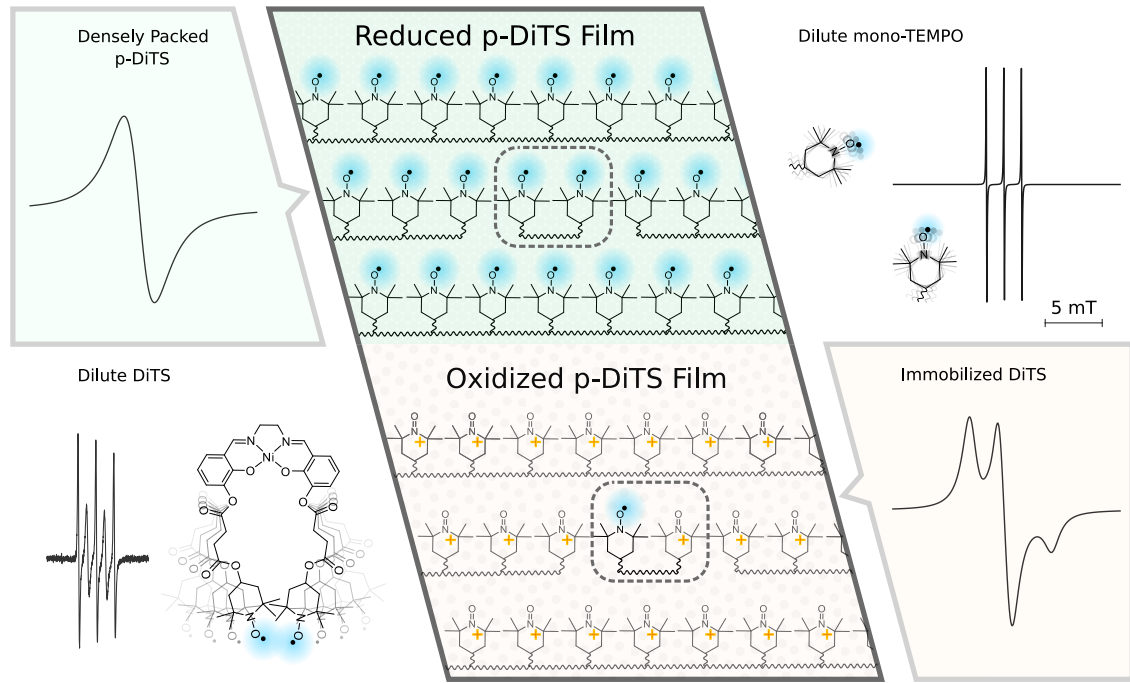


Figure 3.15: Classification of the nitroxide cwEPR spectra observed for p-DiTS under different conditions and in different environments. a): Densely packed nitroxide film with dipolar broadening and exchange narrowing or broadening giving a single derivative line. b): Typical spectrum of dilute mono-nitroxide in solution, three-lines due to $S = 1/2$, $I = 1$ ^{14}N hyperfine interaction (described by isotropic g -factor and isotropic hyperfine (A) interaction). c): Typical spectrum of tumbling di-nitroxide in solution where dynamic changes in the nitroxide – nitroxide distance modulate the exchange interaction yielding a five-line structure with alternating line width (measured cwEPR of DiTS monomers in solution at room temperature). d): Immobilized nitroxide spectrum with both g and A anisotropy.

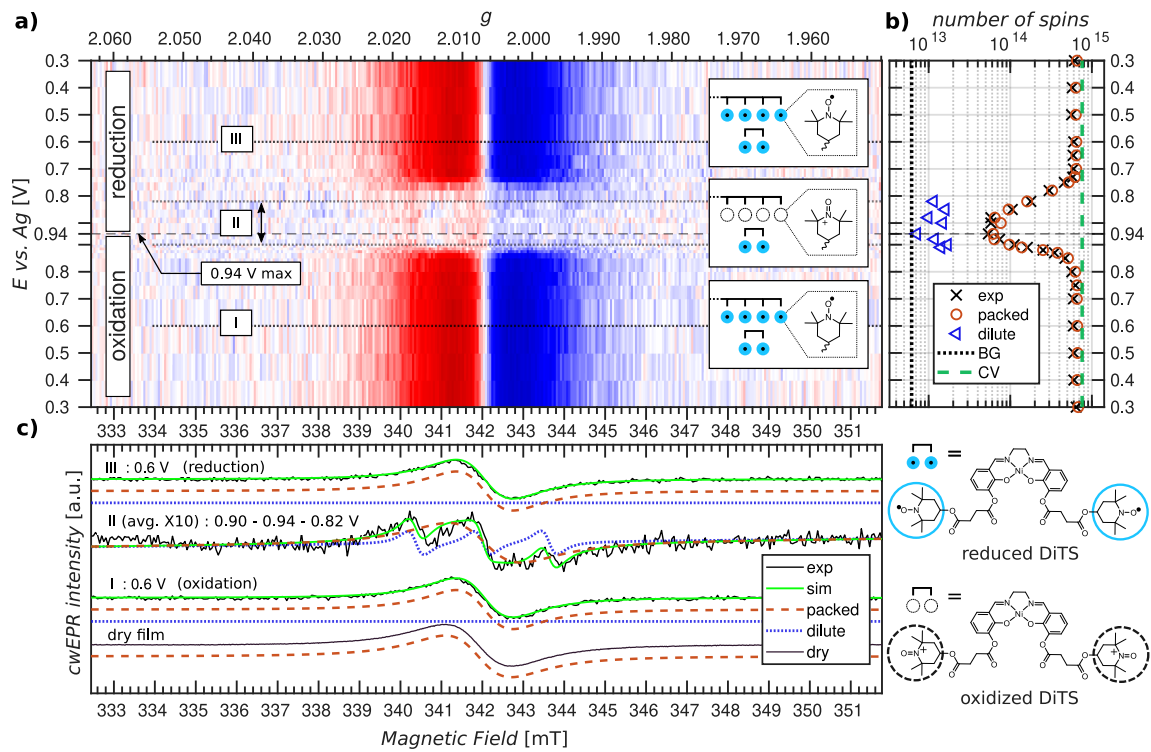


Figure 3.16: XXX

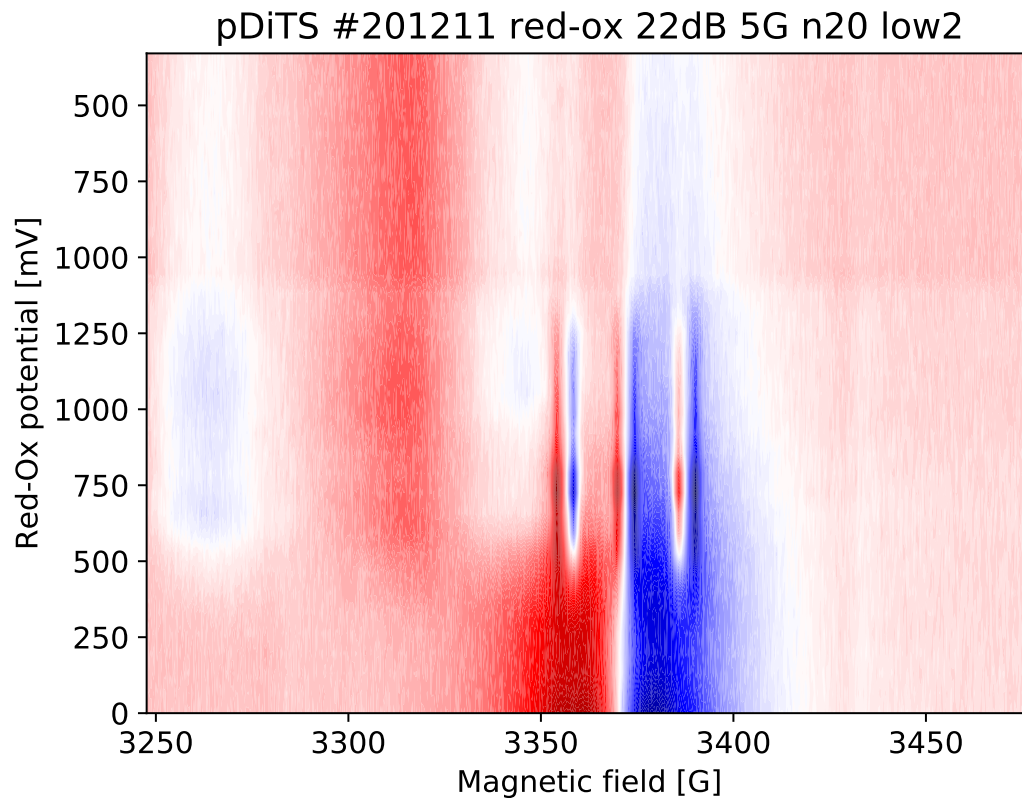


Figure 3.17: Operando cwEPR spectra of a pDiTS electrochemical cell showing irreversible release of charge-bearing fragments and decomposition of the device upon the extreme charging currents.

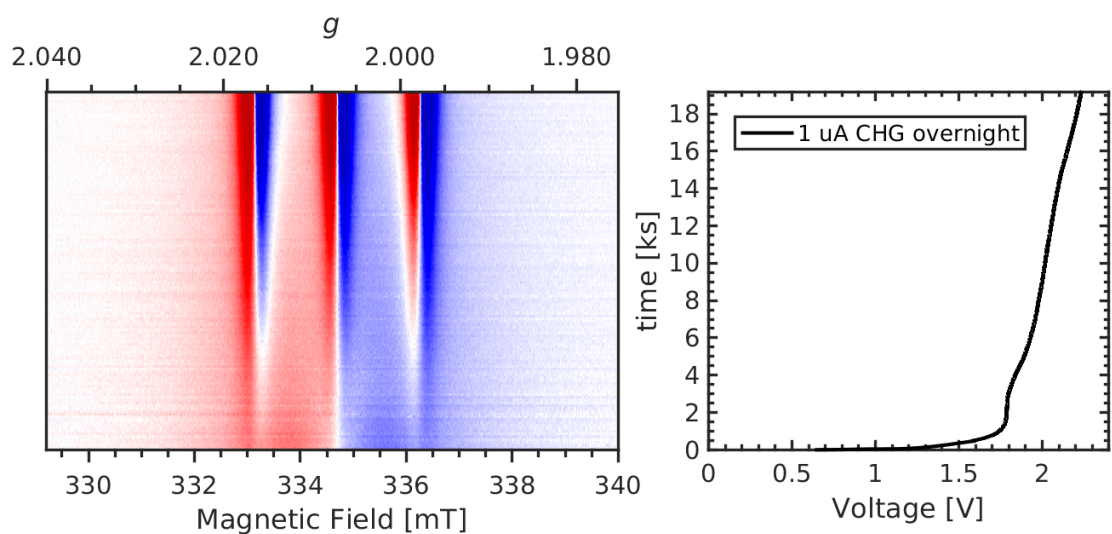


Figure 3.18: Operando cwEPR spectra of a pDiTS electrochemical cell showing irreversible release of charge-bearing fragments upon moderate charging currents.

3.4. VERSATILE ELECTRODE SETUP FOR EX-SITU AND IN-SITU SPECTROELECTROCHEMICAL EPR

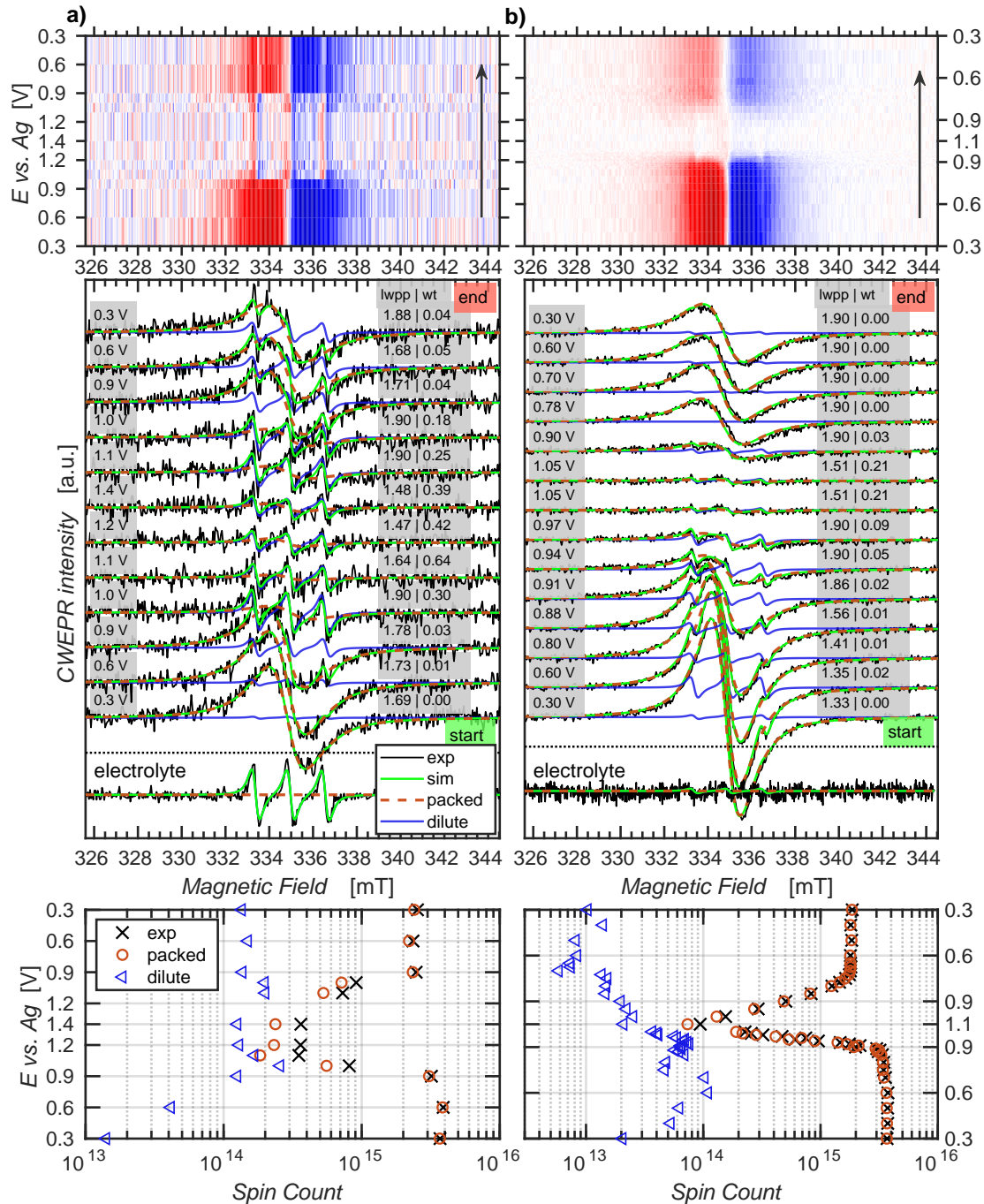


Figure 3.19: Operando cwEPR spectra of two pDiTS electrochemical cells showing release of charge-bearing fragments upon the charge-discharge cycle.

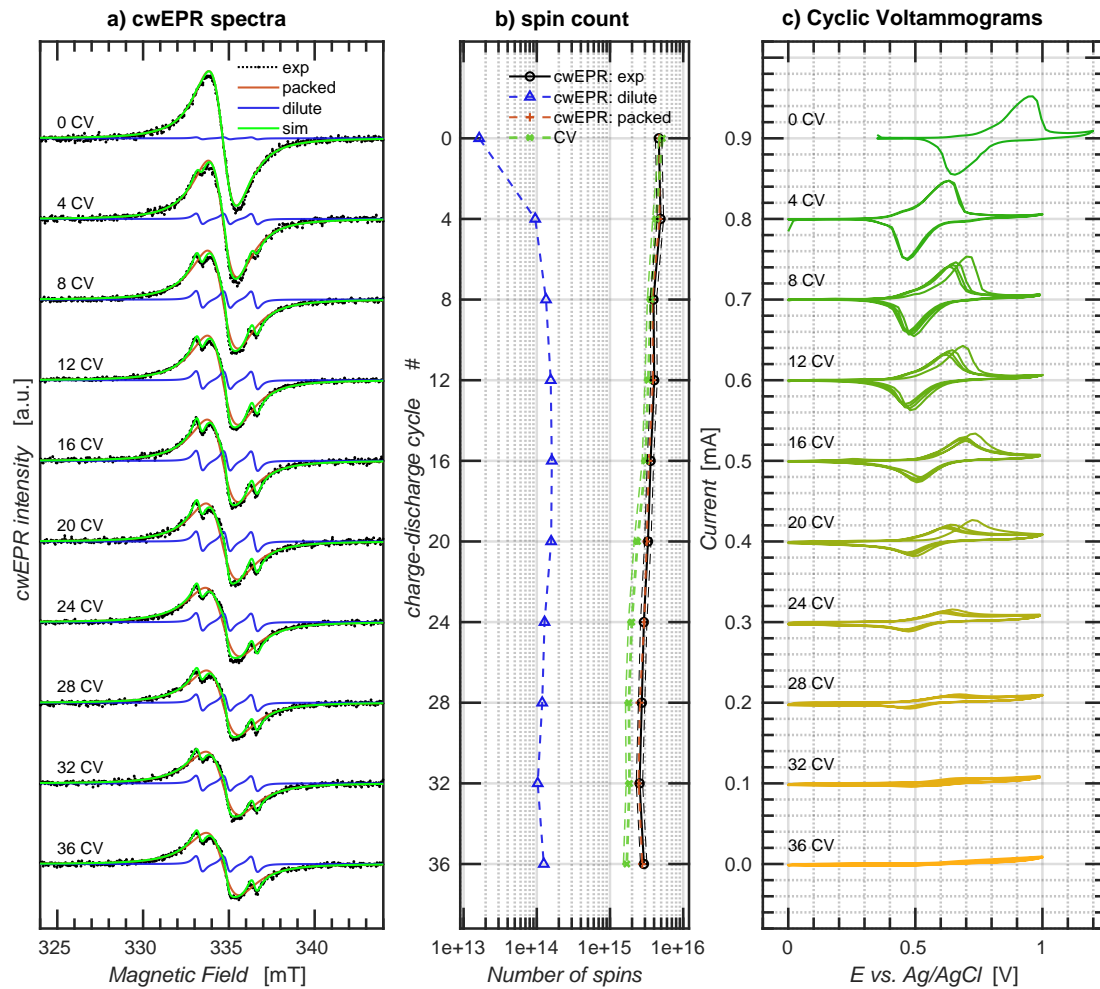


Figure 3.20: ZZZ

3.4. VERSATILE ELECTRODE SETUP FOR EX-SITU AND IN-SITU SPECTROELECTROCHEMICAL EPR

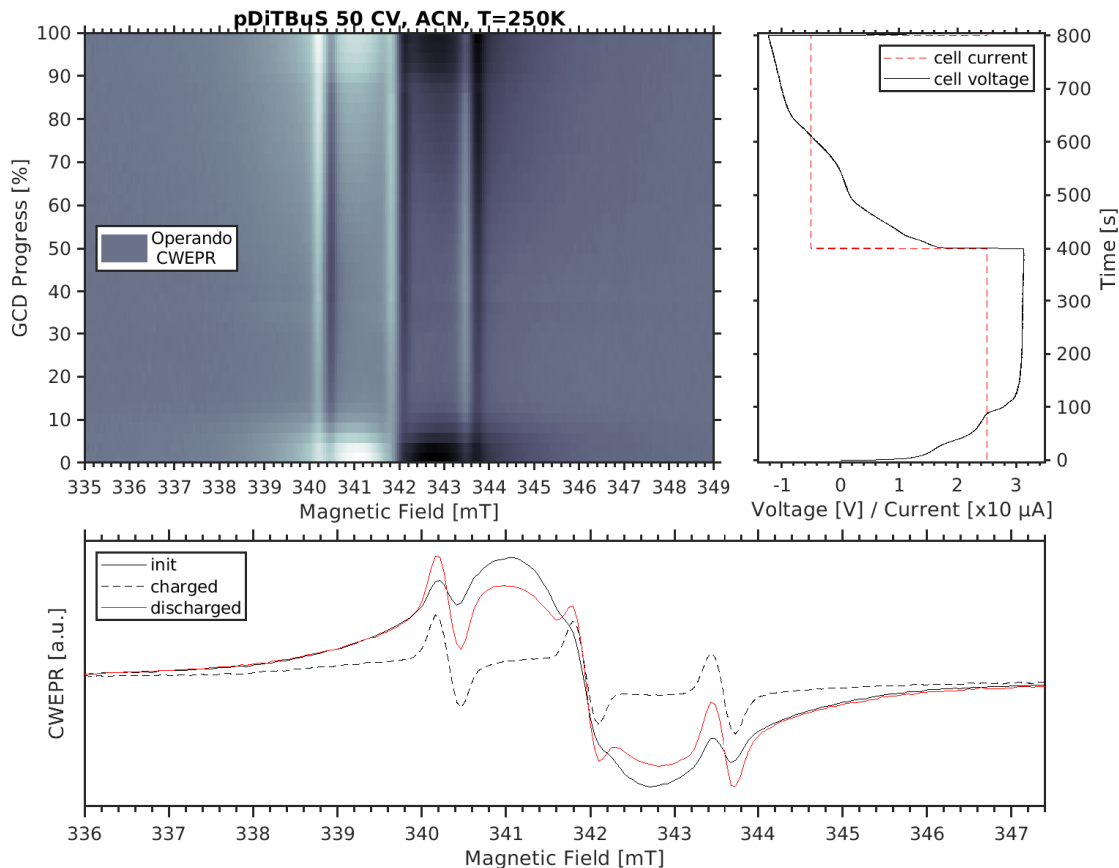


Figure 3.21: XXX

Chapter 4

Pulsed EPR Spectroscopy of TEMPO-containing Battery Cathodes

4.1 Coherent Spin Motion under Pulsed Microwave Field

When a spin system is excited with a microwave pulse, its evolution is described with the set of equations that is known as the Bloch equations.

4.1.1 Bloch Equations

4.1.2 Spin Relaxation Times

4.1.3 Spin Packets

4.2 Instrumentation

4.2.1 Pulse Sequences and Measurement Techniques

The Refocused Spin Echo

The Hahn Echo sequence consists of two pulses, the $\pi/2$ pulse and the π pulse, separated in time by τ : $\pi/2 - \tau - \pi - \tau - echo$. Initially, the macroscopic magnetization of the spin system is aligned along \vec{B}_0 : $\vec{M}_0 = M_Z \vec{e}_Z$. The $\pi/2$ microwave pulse has such length $t_{\pi/2}$ and amplitude B_1 that, during the pulse, \vec{M} nutates to the xy plane, where it keeps precessing about \vec{e}_Z after the end of the pulse. The difference in local environments for each individual spins in the spin packet, as well as the interactions between the spins, that make up \vec{M} , leads to slightly different precession frequencies ω_L^i of the spins. After some

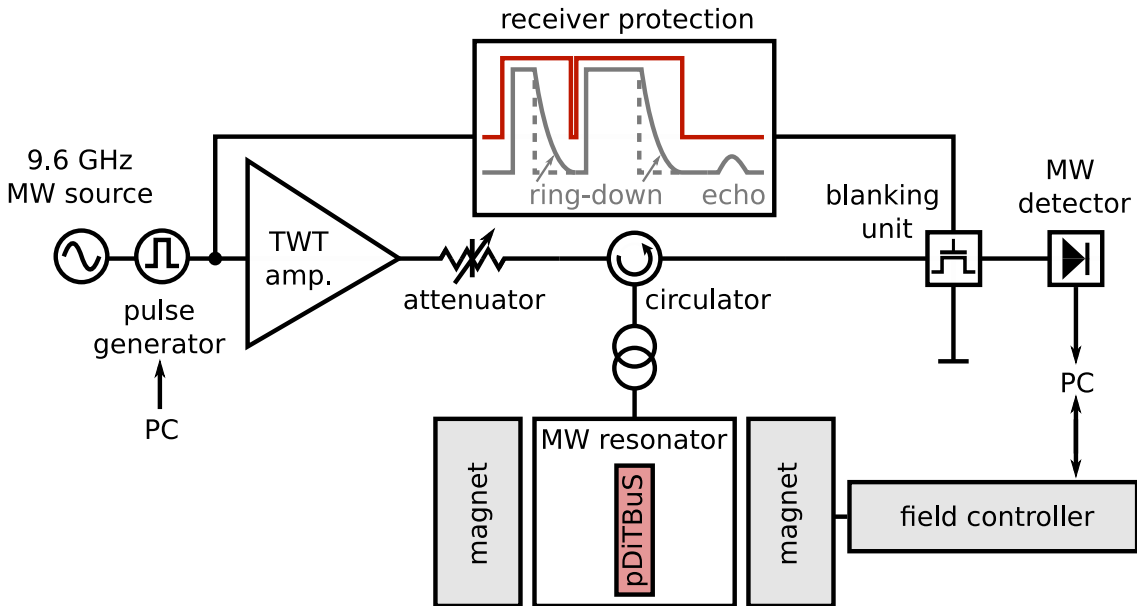


Figure 4.1: Diagram of a pulsed EPR spectrometer.

time τ , the difference in the precession frequencies translates into the differences in phases so that the vector sum of the excited spins averages down to $\vec{0}$ for sufficiently long τ . In other words, the excited spin packet dephases with time. The dephasing due to different local spin environments can be reversible if the deviations of the precession frequencies do not depend on time, as is the case for separated electrons in an inhomogeneous solid. In such case, a π pulse can be applied to the spin system to flip every single spin in the dephased spin packet by 180deg in a plane containing \vec{e}_Z , so that the spins keep precessing in the xy plane, but the direction of precession is inverted for them, leading to the effect that is opposite to the initial dephasing. So a τ after the π pulse excites the spin packet, the accumulated phase differences become the smallest and the packet recovers its macroscopic magnetization \vec{M} that oscillates in the xy plane with $\langle \omega_L^i \rangle$ and can be detected. The recovered \vec{M} at $t = \tau$ after the π pulse is called the refocused spin echo. The difference in ω_L^i leads to a further dephasing of the considered spin packet and to the vanishing of \vec{M} .

Spin Echo Decay and Phase Memory Time

Inversion Recovery and Spin-Lattice Relaxation Time

4.2.2 Broad-Band Excitation and Instantaneous Diffusion

In Section /// it is shown that in a densely packed radical system, as in a TEMPO-Salen cathode film, the phase memory time can be shorter than $T_m \leq 100$ ns. That is, the spin echo is decaying by $e \approx 3$ at $t = 100$ ns. The short phase memory time limits the duration of the pulse sequence at which the echo is detectable. For a $\pi/2 - \tau - \pi - \tau - \text{echo}$ sequence, with a hardware limitation on $\tau \geq t_d \approx 100$ ns, the shorter pulse sequence becomes longer than $t > 200$ ns. By this time, the spin echo decreases by $e^2 \approx 7$ and may be comparable to noise. The limitations imposed by the finite T_m and t_d force one to use shorter microwave pulses.

A short microwave pulse may have a spectral width comparable to the width of the observed spectrum. According to the Fourier theorem, the spectral width of a pulse is inversely proportional to the pulse length: $\Delta\omega \sim 1/t_p$. A spectrum of a 100 ns long rectangular pulse shown in Figure /// is ///MHz wide (FWHM).

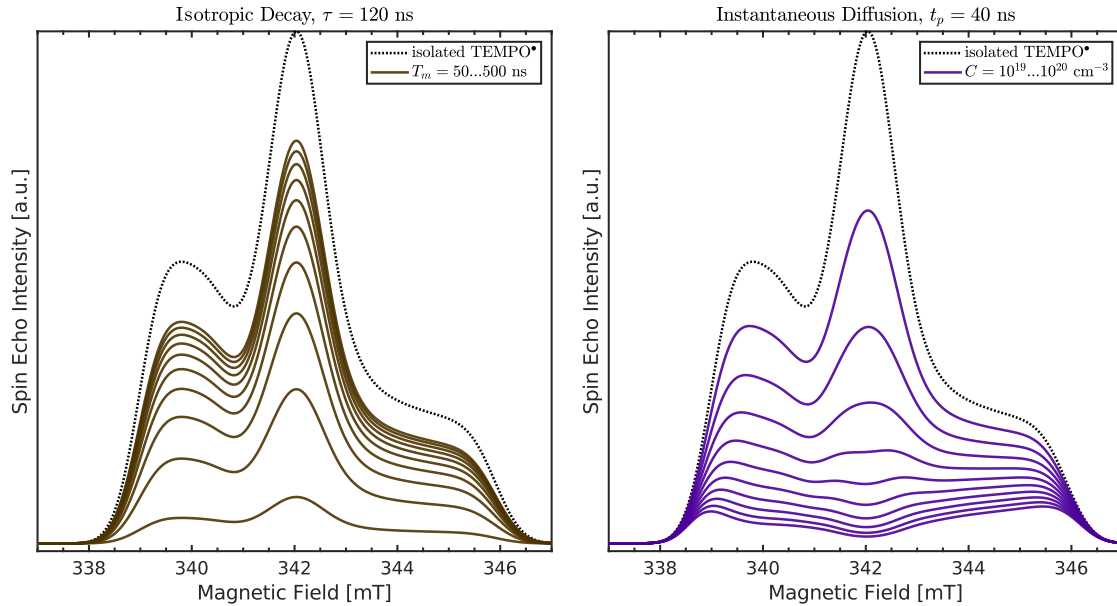


Figure 4.2: Distortions of a nitroxide FSE spectrum caused by isotropic spin relaxation (left) and instantaneous diffusion (right).

4.3 Pulsed EPR Spectroscopy of a charged pDiTBuS Cathode film

4.3.1 Field Swept Echo of a charged pDiTBuS Cathode film

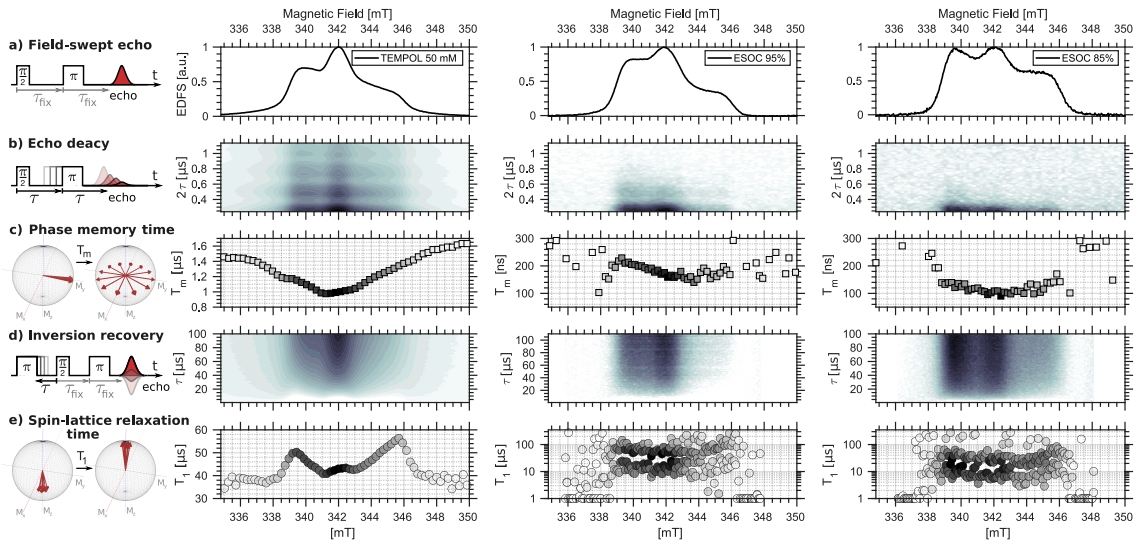


Figure 4.3: XXX

4.3.2 Estimation of Local Spin Concentrations with Instantaneous Diffusion

4.3.3 Spin Relaxation in a charged pDiTBuS Cathode Film

4.4 Padé-Laplace Deconvolution of Polyexponential Decay Signals

The echo decay and inversion recovery transients measured in the corresponding experiments may contain multiple exponential decay components. The conventional method of determining the distribution of the decay components in a transient decay is the Laplace inversion, where the signal in the time domain $s(t)$ is converted into its Laplace image

$$L(p) = \int_0^{+\infty} s(t)e^{-pt}dt$$

in the time-constant domain $p = 1/t$, where the peaks of $L(p)$ give

the decay constants that make up the signal. However, for the noisy signal, the direct calculation of the Laplace transform brings in artifacts that drastically vary with the noise. The signal-to-noise ratio (SNR) of the recorded data makes it difficult to apply the Laplace inversion to determine the number of the decay components, as the Laplace transform is unstable at that SNR.

The Padé-Laplace method comes useful for analyzing noisy polyexponential decays as it was demonstrated in Ref. [24]. The idea of the Padé-Laplace method is to analyze the Padé approximation of the Taylor expansion of the $L(p)$ in the vicinity of one of the expected decay constants p_0 , rather than considering the $L(p)$ fully. This way of signal decomposition is stable against the noise for SNR<10 (see Figure 4.4). The number of exponents detected by the Padé-Laplace method as well as their locations in the p space may vary depending on the expansion point p_0 . We considered $p_0 = 1/t_{1/2}$ where $t_{1/2}$ is the time at which the signal amplitude halves.

We implemented the following algorithm to detect the number of exponents in the decaying transient $s(t)$:

First, a point $p_0 = 1/t_{1/2}$ was chosen, at which $s(t)$ halves.

Then, 11 coefficients of the Taylor expansion of the Laplace transform $L(p)$ were calculated in the vicinity of $p \rightarrow p_0$

$$L(p)|_{p \rightarrow p_0} = \sum_{n=0}^{11} d_i (p - p_0)^i \quad (4.1)$$

with

$$d_i = \frac{1}{i!} \left(\frac{d^{(i)} L}{dp^{(i)}} \right)_{p=p_0} \quad (4.2)$$

where the derivatives $\frac{d^{(i)} L}{dp^{(i)}}$ are computed numerically at the point $p = p_0$ from the discrete signal $s(t) = (t_j, f_j)$, $j = 1 \dots M$:

$$\frac{d^{(i)} L}{dp^{(i)}} = \sum_{j=2}^{M-1} (-t_j)^i e^{(-p_0 t_j)} f_j + \frac{1}{2} \left((-t_1)^i e^{(-p_0 t_1)} f_1 + (-t_M)^i e^{(-p_0 t_M)} f_M \right) \quad (4.3)$$

Then the Taylor expansion for $L(p)$ was approximated in the vicinity of p_0 with the Padé polynomials $a(p)$ and $b(p)$ of orders $n = 5$ and $n = 6$ respectively:

$$L(p)|_{p \rightarrow p_0} = d_0 + d_1(p - p_0) + \dots + d_{11}(p - p_0)^{11} = \frac{a_0 + a_1(p - p_0) + \dots + a_5(p - p_0)^5}{1 + b_1(p - p_0) + \dots + b_6(p - p_0)^6} \quad (4.4)$$

The equation 4.4 is multiplied by the denominator and the prefactors at $(p - p_0)^n$ for $n = 6 \dots 11$ are compared. This defines a system of linear equations on coefficients b_i :

$$\begin{pmatrix} d_5 & d_4 & d_3 & d_2 & d_1 & d_0 \\ d_6 & d_5 & d_4 & d_3 & d_2 & d_1 \\ d_7 & d_6 & d_5 & d_4 & d_3 & d_2 \\ d_8 & d_7 & d_6 & d_5 & d_4 & d_3 \\ d_9 & d_8 & d_7 & d_6 & d_5 & d_4 \\ d_{10} & d_9 & d_8 & d_7 & d_6 & d_5 \end{pmatrix} \begin{pmatrix} b_1 \\ b_2 \\ b_3 \\ b_4 \\ b_5 \\ b_6 \end{pmatrix} = \begin{pmatrix} -d_6 \\ -d_7 \\ -d_8 \\ -d_9 \\ -d_{10} \\ -d_{11} \end{pmatrix} \quad (4.5)$$

From 4.5, b_i are found. The coefficients a_i are found from d and b .

Finally, the Padé approximation $P = \frac{a}{b}$ is constructed and its poles are analyzed. The position of the poles reveal the decay constants. The residues at the poles may give the amplitudes of the decay components, but this was not used in the present study.

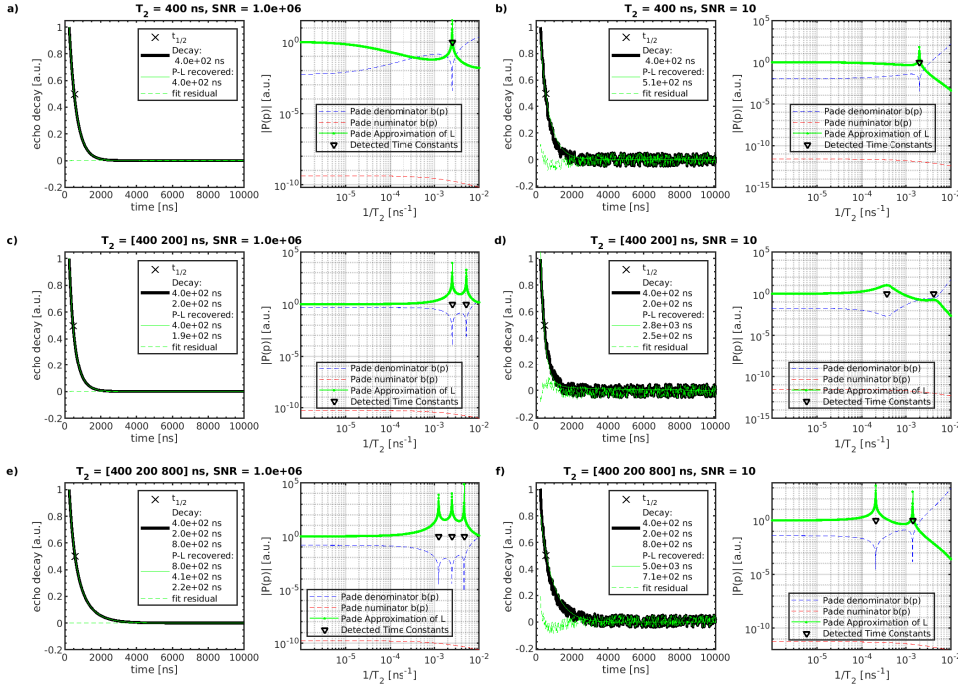


Figure 4.4: Padé-Laplace deconvolution of the mock data containing two decay constants with various signal-to-noise (SNR) ratios.

4.4.1 Padé-Laplace Deconvolution of the Echo-Decay and Inversion-Recovery Transients

We used the Padé-Laplace method to determine the number of the decay constants in the signals and used multiexponential fits to adjust the decay constants and their amplitudes. For the echo decay transients the best fits were monoexponential fits, even though the Padé-Laplace analysis initially showed biexponential behavior for pDiTBuS with major contribution from the fast decay constants in the order of the detector's dead time. All recorded echo decay transients contain oscillations due to the ESEEM effect. The oscillations were excluded from the analysis as shown in the 'fit area' on the plots in Figure 4.6, Figure 4.8 and Figure 4.10.

Echo Decay in 50 mM TEMPOL

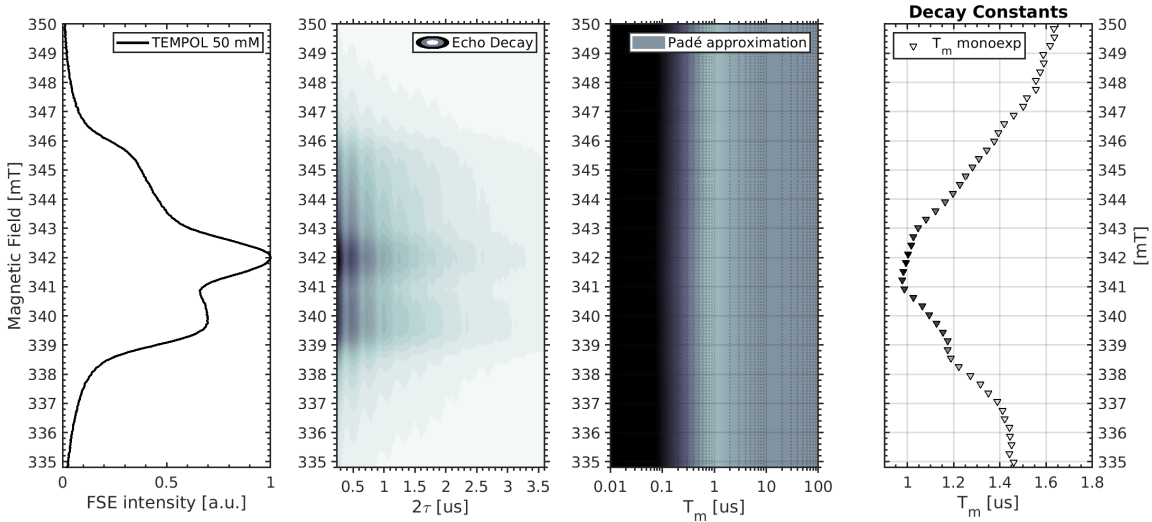


Figure 4.5: Padé-Laplace deconvolution of the field-swept spin echo decay in a frozen 50 mM solution of TEMPOL in Dichloromethane:Acetonitrile glass (3:1). One decay component detected with Padé-Laplace (triangles, right panel). Monoexponential fit (squares for faster component, circles for slower component, right panel). Temperature 5K.

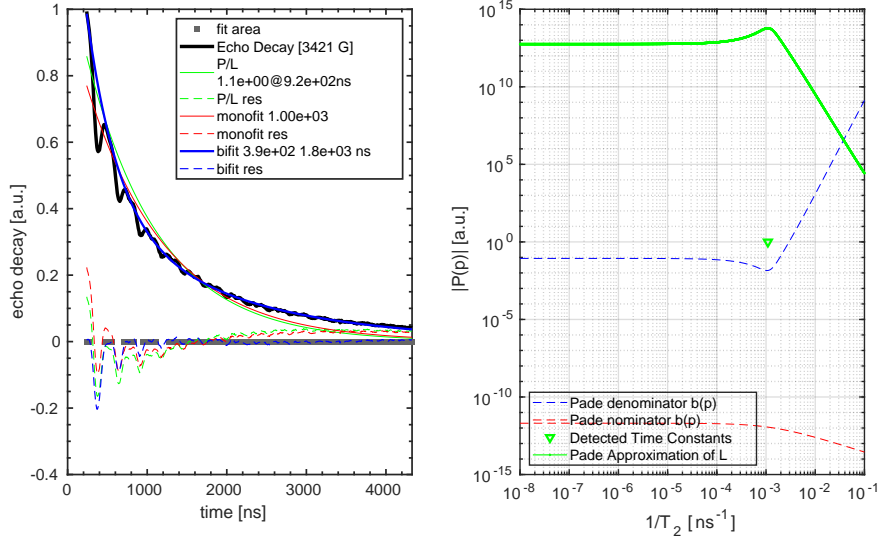


Figure 4.6: Fits of the echo decay transient in the frozen 50 mM TEMPOL solution at the central spectral peak ($m_I = 0$, 342 mT). Padé-Laplace deconvolution the transient vs. free monoexponential fit vs biexponential fit. Temperature 5K. Data was fit in the 'fit area' region. ESEEM oscillations were excluded from the data for fit and Padé-Laplace analysis.

Echo Decay in DiTBuS 95% ESOC

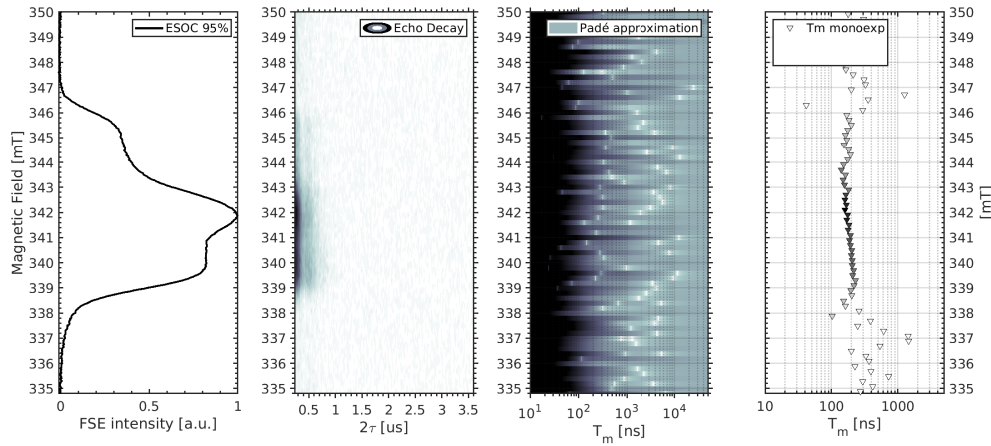


Figure 4.7: Padé-Laplace deconvolution of the field-swept spin echo decay in the pDiTBuS film at 95% ESOC. Temperature 5K.

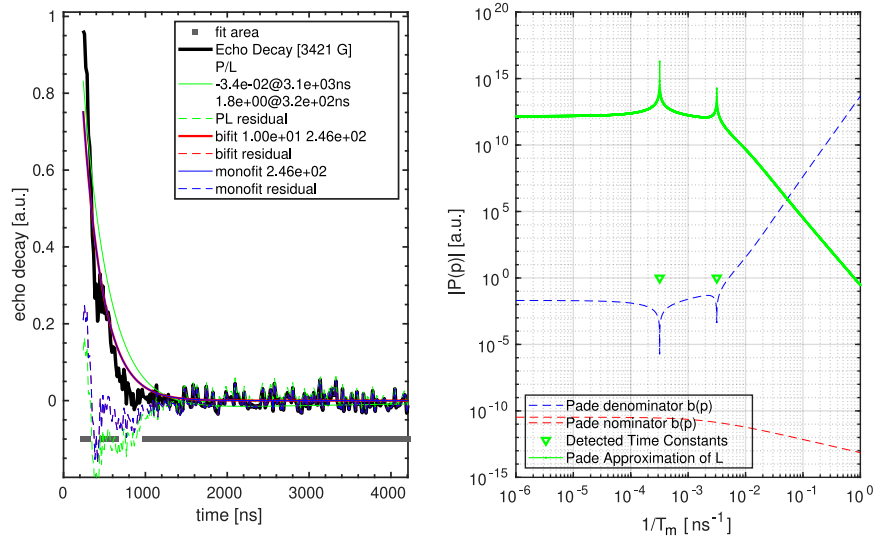


Figure 4.8: Fits of the echo decay transient in the pDiTBuS film at 95% SoC at the central spectral peak ($m_I = 0$, 342 mT). Padé-Laplace deconvolution the transient vs. free mono-exponential fit vs biexponential fit. Temperature 5K. Data was fit in the 'fit area' region. ESEEM oscillations were excluded from the data for fit and Padé-Laplace analysis.

Echo Decay in DiTBuS 85% ESOC

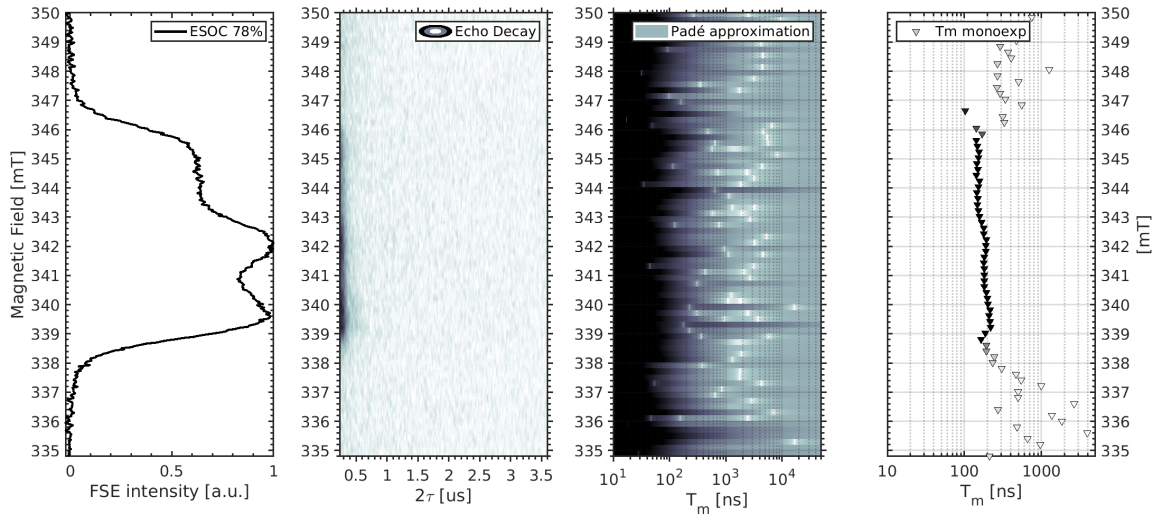


Figure 4.9: Padé-Laplace deconvolution of the field-swept spin echo decay in a pDiTBuS film at 85% ESOC. Temperature 5K.

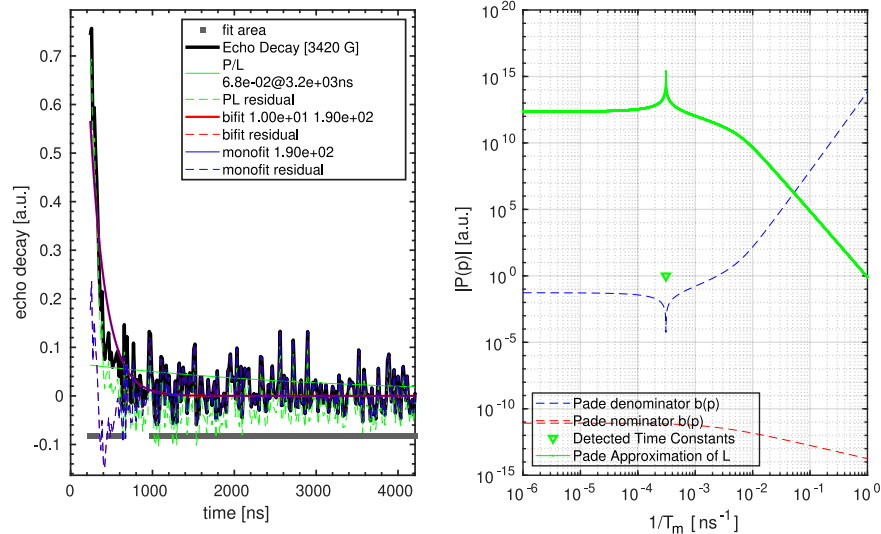


Figure 4.10: Padé-Laplace deconvolution, biexponential and monoexponential fits of the spin echo decay in a pDiTBuS film at 85% SoC at the $m_I = 0$ spectral position. Temperature 5K. Data was fit in the 'fit area' region. ESEEM oscillations were excluded from the data for fit and Padé-Laplace analysis.

Inversion Recovery in 50 mM TEMPOL

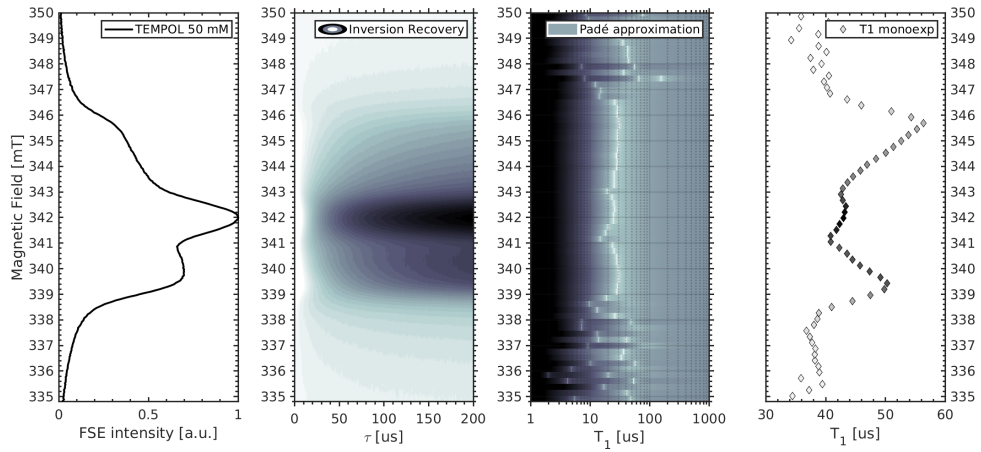


Figure 4.11: Padé-Laplace deconvolution of the field-swept inversion recovery in a frozen 50 mM solution of TEMPOL in the Dichloromethane:Acetonitrile glass (3:1). Two decay components detected with Pade-Laplace (separated poles in the Padé-Laplace approximation, third panel). Biexponential fit (circles for faster component, squares for slower component, right panel). Temperature 5K.

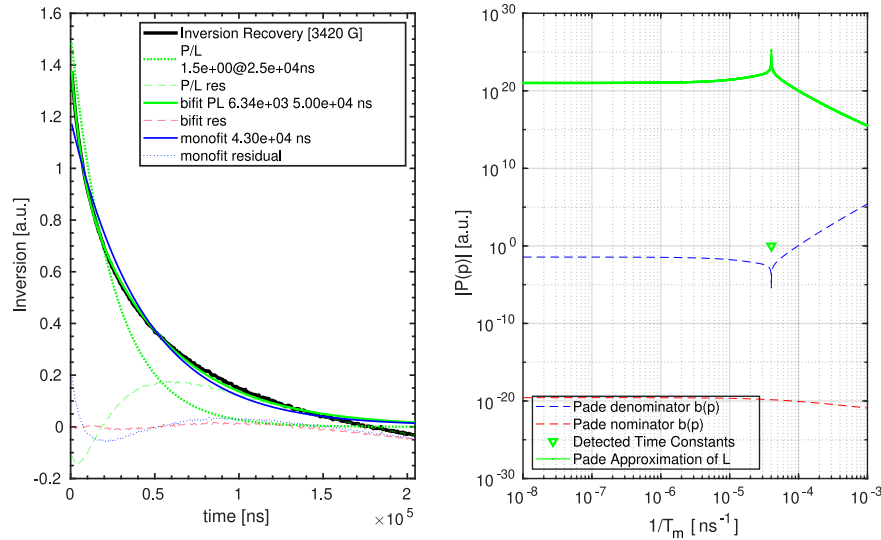


Figure 4.12: Fits of the inversion recovery transient in the frozen 50 mM TEMPOL solution at the central spectral peak ($m_I = 0$, 342 mT). Padé-Laplace deconvolution the transient and a biexponential fit. Temperature 5K.

Inversion Recovery in DiTBuS 95% ESOC

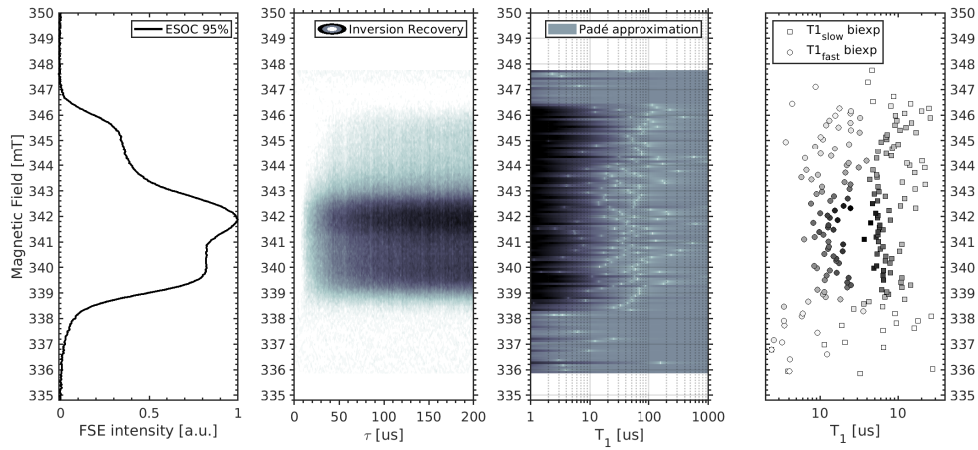


Figure 4.13: Padé-Laplace deconvolution of the field-swept inversion recovery in a pDiT-BuS film at 95% ESOC. Temperature 5K.

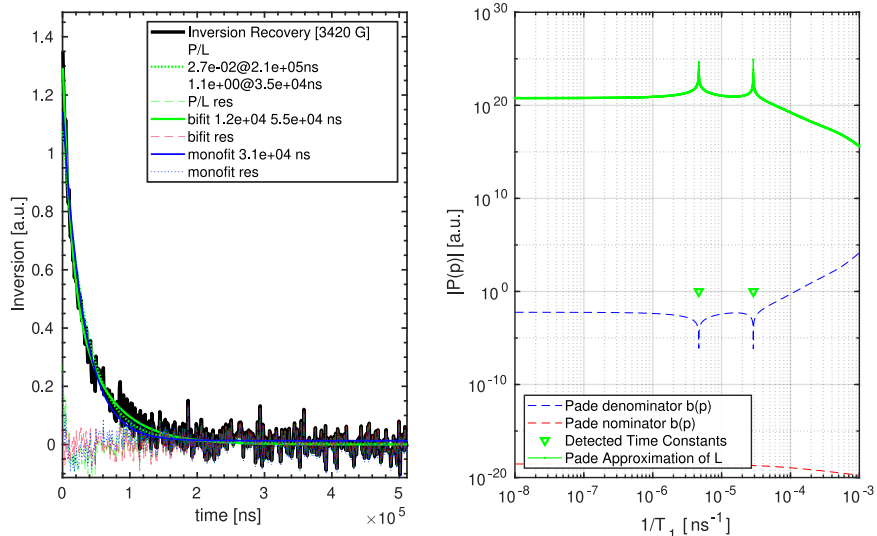


Figure 4.14: Fits of the inversion recovery transient in the 95% ESOC pDiTBuS film at the central spectral peak ($m_I = 0$, 342 mT). Padé-Laplace deconvolution the transient and a biexponential fit. Temperature 5K.

Inversion Recovery in DiTBuS 85% ESOC

4.4.2 Detection of Domains with Poor Conductivity

4.4.3 Towards Electron Resonance Imaging of Spin Concentrations in Battery Electrodes

The local spin concentrations that are present in an electrode film can be obtained by the time-constant-domain analysis of the echo decay transients, as it was described in 4.4.2.

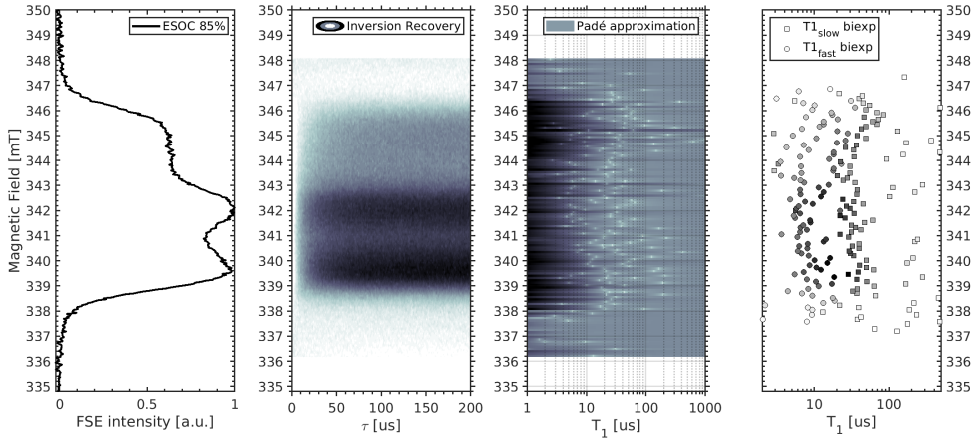


Figure 4.15: Padé-Laplace deconvolution of the field-swept inversion recovery in a pDiT-BuS film at 85% ESOC. Temperature 5K.

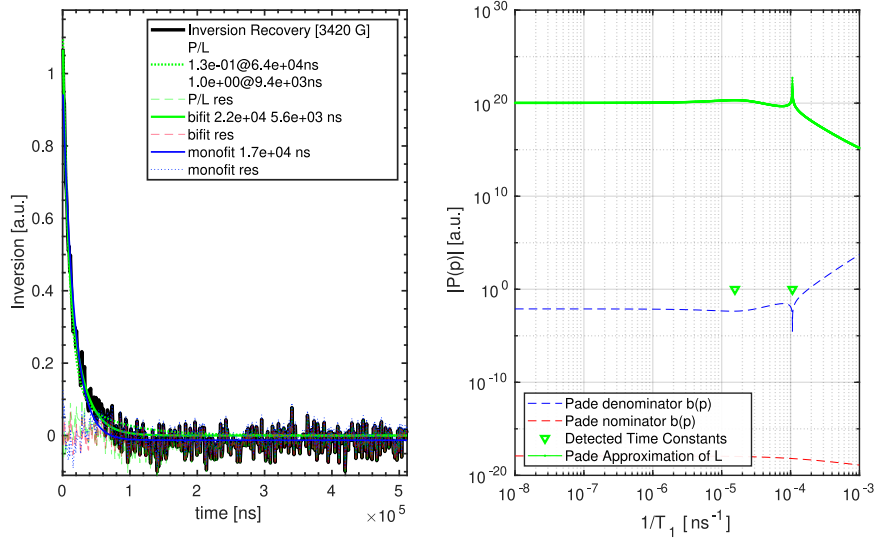


Figure 4.16: Padé-Laplace deconvolution and biexponential fit of the inversion recovery in a pDiT_{BuS} film at 85% ESOC at the $m_I = 0$ spectral position. Temperature 5K. Data is inverted and scaled before fitting.

One can extend this characterization technique and obtain a spatially resolved image of the spin concentrations inside the battery electrode by encoding the position at which the sample is excited with a gradient of the magnetic field. A strongly asymmetric ferromagnetic

wedge [20] can be used to superimpose a gradient of B_0 in a chosen direction so one can not only measure the spin concentrations that are present in the electrode, but also to locate the electrochemically inactive domains and to visualize the conductive paths throughout the electrode, analogously to the NMR imaging. The difficulty on the way to apply this visualization technique lies in the large excitation bandwidth of the pulse sequence.

Let the cathode film of width l be oriented along the static magnetic field so that B_0 lies in the film plane. Let the B_0 be fixed at the maximum intensity of the FSE spectrum, say, $B_0 = B_0^{res} = 342$ mT. Let B_0 be homogeneous within the film length, which is normally the case for the EPR resonator. Let the film contain a distribution of spin concentrations within its length $C_{min} < C(z) < C_{max}$. With the homogeneous B_0 , the microwave pulse will excite the entire film length and the spin echo signal will contain spin echoes from all length elements of the film, that correspond to all $C(z)$. The inversion recovery transient will contain the time constants from all length elements of the film $T_1(z)$. With the Padé-Laplace analysis one recovers the distribution of the concentrations within the film C_i , but since the B_0 is homogeneous, the information on the position z_i at which the domains are located, is lost.

Let now the B_0 to be linearly increasing from $B_0(z = -l/2) = B_0^{res} - \Delta B_0$ at one side of the film to $B_0(z = l/2) = B_0^{res} + \Delta B_0$ by the other side of the film, so that for a given length element dl the inhomogeneity of B_0 is $dB/dl = \frac{B(z=l/2)-B(z=-l/2)}{l}$. In the center of the film (at $z = 0$) the B_0 is resonant and the spin echo signal will be generated, while from the other positions of the film the magnetic field will be non-resonant and no spin echo signal will be generated. Let the width of the EPR spectrum be $\Delta B_{FWHM} = 8$ mT and that to define the probed length element Δl with the given B_0 gradient. $\frac{\Delta B_{FWHM}}{\Delta l} = \frac{B(z=l/2)-B(z=-l/2)}{l}$, so the spatial resolution is

$$\frac{\Delta l}{l} = \frac{\Delta B_{FWHM}}{B(z = l/2) - B(z = -l/2)} \quad (4.6)$$

With the spectral width of $\Delta B_{FWHM} \leq 8$ mT and the film width of $l \leq 3 \times 10^{-1}$ cm to get 256 points per film length one needs a B_0 gradient of $dB/dl \geq 256 * 8 / 0.3 \geq 6.8$ [T/cm] which is a realistic value for a typical Stern-Gerlach apparatus [20, 42].

Chapter 5

Conclusions and Outlook

What hasn't worked so far is the EDMR. It would be super cool to see the signal, but my devices don't live that long. LOD also did not work up to now. Adjusting the pulse train rate to the eigenfrequency of the ENDOR coils turned out to be an irresistible obstacle.

EDMR is allowing to manipulate the spin of an electron that tunnels through a disordered media such as the amorphous silicon in a solar cell, through intertwined fragments of conjugated polymers in an organic solar cell or an organic field-effect transistor.

Bibliography

- [1] Muhammed Aydin and Burak Esat. A polythiophene derivative bearing two electroactive groups per monomer as a cathode material for rechargeable batteries. *Journal of Solid State Electrochemistry*, 19:2275–2281, 8 2015.
- [2] S Bahceci and B Esat. A polyacetylene derivative with pendant tempo group as cathode material for rechargeable batteries. *Journal of Power Sources*, 242:33–40, 2013.
- [3] Robert Bittl and Stefan Weber. Transient radical pairs studied by time-resolved epr. *Biochimica et Biophysica Acta - Bioenergetics*, 1707:117–126, 2005.
- [4] Enrica Bordignon. Epr spectroscopy of nitroxide spin probes. *eMagRes*, 6:235–254, 2017.
- [5] A Carrington and A. D. McLachlan. *Introduction to Magnetic Resonance with Applications to Chemistry and Chemical Physics*. John Weatherhill, inc, 1969.
- [6] A Carrington and A. D. McLachlan. *Introduction to Magnetic Resonance with Applications to Chemistry and Chemical Physics*. John Weatherhill, inc, 1969.
- [7] Nerea Casado and David Mecerreyes. Chapter 1: Introduction to redox polymers: Classification, characterization methods and main applications, 2021.
- [8] Nerea Casado and David Mecerreyes. *Redox Polymers for Energy and Nanomedicine*. The Royal Society of Chemistry, 2021.
- [9] Harold Cassidy. Electron exchange-polymers. *J. Am. Chem. Soc.*, 71:402–406, 1949.
- [10] Florian Degen and Marius Schütte. Life cycle assessment of the energy consumption and ghg emissions of state-of-the-art automotive battery cell production. *Journal of Cleaner Production*, 330:129798, 2022.

- [11] Boucar Diouf and Christophe Avis. The potential of li-ion batteries in ecowas solar home systems. *Journal of Energy Storage*, 22:295–301, 2019.
- [12] Evgenia Dmitrieva, Marco Rosenkranz, Julia S. Danilova, Evgenia A. Smirnova, Mikhail P. Karushev, Irina A. Chepurnaya, and Aleksander M. Timonov. Radical formation in polymeric nickel complexes with n2o2 schiff base ligands: An in situ esr and uv-vis-nir spectroelectrochemical study. *Electrochimica Acta*, 283:1742–1752, 2018.
- [13] A. Einstein. Relativity the special and general theory, 1921.
- [14] X. Fan, T. G. Myers, B. A.D. Sukra, and G. Gabrielse. Measurement of the electron magnetic moment. *Physical Review Letters*, 130, 2 2023.
- [15] M. Fehr, J. Behrends, S. Haas, B. Rech, K. Lips, and A. Schnegg. Electrical detection of electron-spin-echo envelope modulations in thin-film silicon solar cells. *Physical Review B - Condensed Matter and Materials Physics*, 84:1–5, 11 2011.
- [16] R P Feynman. Space-time appxoach to quantum electxotiyynamics. *Physical Review*, 76:769–789, 1949.
- [17] Jan Figgener, Peter Stenzel, Kai Philipp Kairies, Jochen Linßen, David Haberschusz, Oliver Wessels, Georg Angenendt, Martin Robinius, Detlef Stolten, and Dirk Uwe Sauer. The development of stationary battery storage systems in germany – a market review. *Journal of Energy Storage*, 29, 6 2020.
- [18] C Fribe and U S Schubert. High-power-density organic radical batteries. *Topics in Current Chemistry*, 375:1–35, 2017.
- [19] Yangyang Fu, Song Lu, Kaiyuan Li, Changchen Liu, Xudong Cheng, and Heping Zhang. An experimental study on burning behaviors of 18650 lithium ion batteries using a cone calorimeter. *Journal of Power Sources*, 273:216–222, 1 2015.
- [20] Walther Gerlach and Otto Stern. Der experimentelle nachweis der richtungsquantelung im magnetfeld. *Zeitschrift für Physik*, 9:348–352, 1922.
- [21] Nicolas Goujon, Nerea Casado, Nagaraj Patil, Rebeca Marcilla, and David Mecerreyes. Organic batteries based on just redox polymers: Abstract. *Progress in Polymer Science*, 122:101449, 2021.

- [22] Cristina Grosu, Chiara Panosetti, Steffen Merz, Peter Jakes, Stefan Seidlmayer, Sebastian Matera, Rüdiger a Eichel, Josef Granwehr, and Christoph Scheurer. Revisiting the storage capacity limit of graphite battery anodes : Spontaneous lithium overintercalation at ambient pressure. *PRX Energy*, 2:1–14, 2023.
- [23] Ting Guan, Shun Sun, Fengbin Yu, Yunzhi Gao, Peng Fan, Pengjian Zuo, Chunyu Du, and Geping Yin. The degradation of LiCoO_2 /graphite batteries at different rates. *Electrochimica Acta*, 279:204–212, 2018.
- [24] Edward H. Hellen. Padé-laplace analysis of signal averaged voltage decays obtained from a simple circuit. *American Journal of Physics*, 73:871–875, 9 2005.
- [25] Takuma Hirasawa, Mika Yoshida, and Shin'ya Obara. Battery control for leveling the amount of electricity purchase in smart-energy houses. *International Journal of Energy Research*, 45:807–823, 2021.
- [26] Q Huang, E D Walter, L Cosimbescu, D Choi, and J P Lemmon. In situ electrochemical-electron spin resonance investigations of multi-electron redox reaction for organic radical cathodes. *Journal of Power Sources*, 306:812–816, 2016.
- [27] T Janoschka, M D Hager, and U S Schubert. Powering up the future: Radical polymers for battery applications. *Adv. Mater.*, 24:6397–6409, 2012.
- [28] Tobias Janoschka, Christian Friebe, Martin D. Hager, Norbert Martin, and Ulrich S. Schubert. An approach toward replacing vanadium: A single organic molecule for the anode and cathode of an aqueous redox-flow battery. *ChemistryOpen*, 6:216–220, 2017.
- [29] Tobias Janoschka, Christian Friebe, Martin D. Hager, Norbert Martin, and Ulrich S. Schubert. An approach toward replacing vanadium: A single organic molecule for the anode and cathode of an aqueous redox-flow battery. *ChemistryOpen*, 6:216–220, 2017.
- [30] G Jeschke. Deer distance measurements on proteins. *Annual Review of Physical Chemistry*, Vol 63, 63:419–446, 2012.
- [31] Josef Kadlec, Radoslav Cipin, Dalibor Cervinka, Pavel Vorel, and Bohumil Klima. Li-ion accumulators for propulsion system of electric airplane vut 051 ray. *Journal of Solid State Electrochemistry*, 18:2307–2313, 2014.

- [32] M Khodeir, B Ernould, J Brassinne, S Ghiassinejad, H Jia, S Antoun, C Fribe, U S Schubert, Z Kochovski, Y Lu, E Van Ruymbeke, and J F Gohy. Synthesis and characterisation of redox hydrogels based on stable nitroxide radicals. *Soft Matter*, 15:6418–6426, 2019.
- [33] Jihyeon Kim, Youngsu Kim, Jaekyun Yoo, Giyun Kwon, Youngmin Ko, and Kisuk Kang. Organic batteries for a greener rechargeable world. *Nature Reviews Materials*, 8:54–70, 2023.
- [34] H Koezuka, A Tsumura, and T Ando. Field-effect transistor with polythiophene thin film, 1987.
- [35] Ilia Kulikov, Naitik A. Panjwani, Anatoliy A. Vereshchagin, Domenik Spallek, Daniil A. Lukianov, Elena V. Alekseeva, Oleg V. Levin, and Jan Behrends. Spins at work: probing charging and discharging of organic radical batteries by electron paramagnetic resonance spectroscopy. *Energy and Environmental Science*, 15:3275–3290, 2022.
- [36] Ilya Kuprov. *Spin: From Basic Symmetries to Quantum Optimal Control*. Springer International Publishing, 1 2023.
- [37] T. Kushida and J. C. Murphy. Volume dependence of the knight shift in lithium. *Physical Review B*, 21:4247–4250, 1980.
- [38] Fredrik Larsson, Petra Andersson, Per Blomqvist, and Bengt Erik Mellander. Toxic fluoride gas emissions from lithium-ion battery fires. *Scientific Reports*, 7:1–13, 12 2017.
- [39] C H Lee, G Yu, D Moses, K Pakbaz, C Zhang, N S Sariciftci, A J Heeger, and F Wudl. Sensitization of the photoconductivity of conducting polymers by c60: Photoinduced electron transfer, 1993.
- [40] Yong Hee Lee, Joo Seong Kim, Jonghyeon Noh, Inhwa Lee, Hyeong Jun Kim, Sunghun Choi, Jeongmin Seo, Seokwoo Jeon, Taek Soo Kim, Jung Yong Lee, and Jang Wook Choi. Wearable textile battery rechargeable by solar energy. *Nano Letters*, 13:5753–5761, 2013.
- [41] Chao Li, Ming Shen, and Bingwen Hu. Solid-state nmr and epr methods for metal ion battery research. *Wuli Huaxue Xuebao/Acta Physico - Chimica Sinica*, 36:1–16, 2019.

- [42] Jiahao Liang, Thomas M. Fuchs, Rolf Schäfer, and Vitaly V. Kresin. Strong permanent magnet gradient deflector for stern-gerlach-type experiments on molecular beams. *Review of Scientific Instruments*, 91, 5 2020.
- [43] Xiangli Liu, Yougang Mao, Errol V. Mathias, Collin Ma, Osmundo Franco, Yong Ba, Julia A. Kornfield, Tieli Wang, Lijun Xue, Bing Sen Zhou, and Yun Yen. Study the property of double-ended fluoroalkyl poly(ethylene glycol) hydrogel as a depot for hydrophobic drug delivery using electron paramagnetic resonance technique and cell proliferation assay. *Journal of Sol-Gel Science and Technology*, 45:269–278, 3 2008.
- [44] Yong Lu and Jun Chen. Prospects of organic electrode materials for practical lithium batteries. *Nature Reviews Chemistry*, 4:127–142, 2020.
- [45] Tianyi Ma, Siyuan Wu, Fang Wang, Joseph Lacap, Chunjing Lin, Shiqiang Liu, Mohan Wei, Weijian Hao, Yunshi Wang, and Jae Wan Park. Degradation mechanism study and safety hazard analysis of overdischarge on commercialized lithium-ion batteries. *ACS Applied Materials and Interfaces*, 12:56086–56094, 2020.
- [46] Praveen Kumar Reddy Maddikunta, Gautam Srivastava, Thippa Reddy Gadekallu, Natarajan Deepa, and Prabadevi Boopathy. Predictive model for battery life in iot networks. *IET Intelligent Transport Systems*, 14:1388–1395, 2020.
- [47] Christoph Meier, Jan Behrends, Christian Teutloff, Oleksandr Astakhov, Alexander Schnegg, Klaus Lips, and Robert Bittl. Multi-frequency edmr applied to microcrys-talline thin-film silicon solar cells. *Journal of Magnetic Resonance*, 234:1–9, 2013.
- [48] Alice J. Merryweather, Quentin Jacquet, Steffen P. Emge, Christoph Schnedermann, Akshay Rao, and Clare P. Grey. Operando monitoring of single-particle kinetic state-of-charge heterogeneities and cracking in high-rate li-ion anodes. *Nature Materials*, 21:1306–1313, 2022.
- [49] S Muench, A Wild, C Fribe, B Haupler, T Janoschka, and U S Schubert. Polymer-based organic batteries. *Chemical Reviews*, 116:9438–9484, 2016.
- [50] K Nakahara, S Iwasa, M Satoh, Y Morioka, J Iriyama, M Suguro, and E Hasegawa. Rechargeable batteries with organic radical cathodes. *Chem. Phys. Lett.*, 359:351–354, 2002.
- [51] Arvid Niemöller, Peter Jakes, Rüdiger A. Eichel, and Josef Granwehr. In operando epr investigation of redox mechanisms in licoo₂. *Chemical Physics Letters*, 716:231–236, 2019.

- [52] Arvid Niemöller, Peter Jakes, Svitlana Eurich, Anja Paulus, Hans Kungl, Rüdiger A. Eichel, and Josef Granwehr. Monitoring local redox processes in $\text{LiNi}_0.5\text{Mn}_1.5\text{O}_4$ battery cathode material by *in operando* epr spectroscopy. *Journal of Chemical Physics*, 148:1–10, 2018.
- [53] H Nishide, S Iwasa, Y J Pu, T Suga, K Nakahara, and M Satoh. Organic radical battery: nitroxide polymers as a cathode-active material. *Electrochimica Acta*, 50:827–831, 2004.
- [54] Hiroyuki Nishide, Kenichiroh Koshika, and Kenichi Oyaizu. Environmentally benign batteries based on organic radical polymers. volume 81, pages 1961–1970, 2009.
- [55] Naoki Nitta, Feixiang Wu, Jung Tae Lee, and Gleb Yushin. Li-ion battery materials: Present and future. *Materials Today*, 18:252–264, 2015.
- [56] Rikard Owenius, Maria Engström, Mikael Lindgren, and Martina Huber. Influence of solvent polarity and hydrogen bonding on the epr parameters of a nitroxide spin label studied by 9-ghz and 95-ghz epr spectroscopy and dft calculations. *Journal of Physical Chemistry A*, 105:10967–10977, 2001.
- [57] Dirac P. A. M. The quantum theory of the electron. *Proceedings of the Royal Society of London. Series A, Containing Papers of a Mathematical and Physical Character*, 117:610–624, 1928.
- [58] Jens F. Peters, Manuel Baumann, Benedikt Zimmermann, Jessica Braun, and Marcel Weil. The environmental impact of li-ion batteries and the role of key parameters – a review. *Renewable and Sustainable Energy Reviews*, 67:491–506, 2017.
- [59] M. H. Poincaré. Sur la dynamique de l'électron. *Rend. Circ. Matem. Palermo*, pages 129–175, 12 1906.
- [60] Anna Pražanová, Vaclav Knap, and Daniel Ioan Stroe. Literature review, recycling of lithium-ion batteries from electric vehicles, part i: Recycling technology. *Energies*, 15:1–29, 2022.
- [61] Kevin J. Rhodes, Roberta Meisner, Melanie Kirkham, Nancy Dudney, and Claus Daniel. In situ xrd of thin film tin electrodes for lithium ion batteries. *Journal of The Electrochemical Society*, 159:A294–A299, 2012.

- [62] Philip Rohland, Erik Schröter, Oliver Nolte, George R. Newkome, Martin D. Hager, and Ulrich S. Schubert. Redox-active polymers: The magic key towards energy storage – a polymer design guideline progress in polymer science, 2 2022.
- [63] K. M. Salikhov, S. A. Dzuba, and A. M. Raitsimring. The theory of electron spin-echo signal decay resulting from dipole-dipole interactions between paramagnetic centers in solids. *Journal of Magnetic Resonance*, 42:255–276, 1981.
- [64] K M Salikhov and N E Zavoiskaya. Zavoisky and the discovery of epr, 2015.
- [65] A Schweiger and G Jeschke. *Principles of Pulse Electron Paramagnetic Resonance*. Oxford University Press, 2001.
- [66] A Schweiger and G Jeschke. *Principles of Pulse Electron Paramagnetic Resonance*. Oxford University Press, 2001.
- [67] J Schwinger. On quantum-electrodynamics and the magnetic moment of the electron. *Physical Review*, 73:416–417, 1948.
- [68] Yongchao Shi and Mingxue Tang. Nmr/epr investigation of rechargeable batteries. *Wuli Huaxue Xuebao/Acta Physico - Chimica Sinica*, 36:1–13, 2019.
- [69] By Hideki Shirakawa, Edwin J Louis, Alan G Macdiarmid, C H W A N K Chi-ang, and Alan J HEEGERt. Synthesis of electrically conducting organic polymers : Halogen derivatives of polyacetylene, (ch), 1977.
- [70] H. Staudinger. Über polymerisation. *European Journal of Inorganic Chemistry*, 53:1073–1085, 6 1920.
- [71] Hiroyuki Takeo Nishide and Suga. Organic radical battery. *Journal of the Society of Mechanical Engineers*, 110:194–195, 2007.
- [72] Yu. V. Toropov, S. A. Dzuba, Yu. D. Tsvetkov, V Monaco, F Formaggio, M Crisma, C Toniolo, and J. Raap. Molecular dynamics and spatial distribution of toac spin-labelled peptaibols studied in glassy liquid by echo-detected epr spectroscopy. *Applied Magnetic Resonance*, 15:237–246, 1998.
- [73] Anatolii. A. Vereshchagin, Daniil A. Lukyanov, Ilia R. Kulikov, Naitik A. Panjwani, Elena A. Alekseeva, Jan Behrends, and Oleg V. Levin. The fast and the capacious: A [ni(salen)]-tempo redox-conducting polymer for organic batteries. *Batteries and Supercaps*, 4:336–346, 2020.

- [74] Anatoliy A. Vereshchagin, Arseniy Y. Kalnin, Alexey I. Volkov, Daniil A. Lukyanov, and Oleg V. Levin. Key features of tempo-containing polymers for energy storage and catalytic systems. *Energies*, 15:1–50, 2022.
- [75] John A. Weil and James R. Bolton. *Electron Paramagnetic Resonance Elementary Theory and Practical Applications*. Wiley, 2nd edition, 2007.
- [76] Y Xie, K Zhang, Y Yamauchi, K Oyaizu, and Z F Jia. Nitroxide radical polymers for emerging plastic energy storage and organic electronics: fundamentals, materials, and applications. *Materials Horizons*, 8:803–829, 2021.
- [77] Yuan Xie, Kai Zhang, Yusuke Yamauchi, Kenichi Oyaizu, and Zhongfan Jia. Nitroxide radical polymers for emerging plastic energy storage and organic electronics: Fundamentals, materials, and applications. *Materials Horizons*, 8:803–829, 2021.
- [78] Chengjian Xu, Qiang Dai, Linda Gaines, Mingming Hu, Arnold Tukker, and Bernhard Steubing. Future material demand for automotive lithium-based batteries. *Communications Materials*, 1:1–10, 2020.
- [79] Hyun Deog Yoo, Elena Markevich, Gregory Salitra, Daniel Sharon, and Doron Aurbach. On the challenge of developing advanced technologies for electrochemical energy storage and conversion. *Materials Today*, 17:110–121, 2014.
- [80] E K Zavoisky. Paramagnetic relaxation of liquid solutions for perpendicular fields. *Zhur. Eksperiment. i Theoret. Fiz.*, 15:344–350, 1945.
- [81] E K Zavoisky. Spin-magnetic resonance in paramagnetics. *Journal of Physics*, 9:245, 1945.
- [82] Clara Zens, Christian Friebe, Ulrich S. Schubert, Martin Richter, and Stephan Kupfer. Tailored charge transfer kinetics in precursors for organic radical batteries – a joint synthetic-theoretical approach. *ChemSusChem*, e202201679:1–14, 2022.
- [83] Guangxu Zhang, Xuezhe Wei, Siqi Chen, Guangshuai Han, Jiangong Zhu, and Haifeng Dai. Investigation the degradation mechanisms of lithium-ion batteries under low-temperature high-rate cycling. *ACS Applied Energy Materials*, 5:6462–6471, 2022.
- [84] Qingsong Zhang, Tiantian Liu, and Qiong Wang. Experimental study on the influence of different heating methods on thermal runaway of lithium-ion battery. *Journal of Energy Storage*, 42:1–9, 10 2021.

- [85] Yiren Zhang, Albert M. Park, Stephen R. McMillan, Nicholas J. Harmon, Michael E. Flatté, Gregory D. Fuchs, and Christopher K. Ober. Charge transport in conjugated polymers with pendent stable radical groups. *Chemistry of Materials*, 30:4799–4807, 7 2018.